

Sheet Metal Blanking Modeling Using Lode-Dependent Plasticity and Ductile Damage Models Combined with 3D Adaptive Remeshing Method

abel cherouat (✉ abel.cherouat@utt.fr)

Université de Technologie de Troyes: Universite de Technologie de Troyes <https://orcid.org/0000-0002-3988-1197>

Jie Zhang

Houman Borouchaki

Research Article

Keywords: Sheet metal blanking, Elastic-visco-plastic, Multi-axial failure, Triaxiality, 3D adaptive remeshing

Posted Date: March 22nd, 2022

DOI: <https://doi.org/10.21203/rs.3.rs-1440979/v1>

License: © ⓘ This work is licensed under a Creative Commons Attribution 4.0 International License.

[Read Full License](#)

Sheet metal blanking modeling using Lode-dependent plasticity and ductile damage models combined with 3D adaptive remeshing method

Abel Cherouat¹, Jie Zhang² and Houman Borouchaki¹

Corresponding author: Abel CHEROUAT

1- UR-GAMMA3, University of technology of Troyes, BP 2060 - 10010 Troyes – France

(abel.cherouat@utt.fr (AC); houman.borouchaki@utt.fr (HB))

2- State Key Laboratory of Metal Matrix Materials Composites, SJTU, sise N° 800, Dongchuan Road, Minhang District, Shanghai – China (email_zhangjie@126.com (JZ))

ABSTRACT. This paper is devoted to numerically study the sheet metal blanking process using elastic-visco-plastic model fully coupled with ductile damage and 3D adaptive remeshing procedure. The proposed constitutive theory aims to capture the effects of irreversible damage associated with the failure mechanisms that occur in sheet metal forming under large deformation. The isotropic ductile damage fully coupled into an elasto-viscoplastic flow stress model and stress state parameters (stress triaxiality and Lode angle) are proposed to control the damage evolution under multi-axial loading path.

When a sheet metal is sheared by large elastic-viscoplastic strains, the propagation of macroscopic cracks induces severe changes of topology and frequent remeshing must be performed in order to avoid large mesh distortion and element quality. An h-adaptive Constraint Delaunay kernel remeshing scheme (refinement and coarsening) dedicated to the simulation of macroscopic ductile cracks initiation and propagation during blanking processes is proposed. Cracks are represented using a procedure based on fully damaged elements deletion. Optimal adaptive element size is driven by error indicators based on both geometrical considerations (tool geometry, deformed part) and the derivatives of physical field (plastic strain or damage localization). The proposed methodology was successfully verified comparing the predicted evolution of material ductility with the experimental data relative to several metals. The procedure for the blanking simulation is also discussed in details.

KEYWORDS: Sheet metal blanking; Elastic-visco-plastic; Multi-axial failure; Triaxiality; 3D adaptive remeshing

1. Introduction

The mechanical engineering industrials increasingly rely on the numerical simulation to design and optimize the metalworking processes. In practice, different simulating processes have different key points needed to be considered specially. In contrast to metal forming processes (casting, forging and sheet metal forming), cutting processes is a term which is used to describe a variety of material removal processes, in which a cutting tool removes unwanted material from a workpiece to produce the desired shape. The sheet metal blanking is one of the material removal processes.

In sheet metal blanking, the ductile damage plays an important role, which makes the prediction of damage evolution become an essential work in numerical simulation. Continuum Damage Mechanics (CDM) is an important theory to predict the ductile damage when material deforms. It assumes that the damage dues to the nucleation and growth of micro defects (voids and cracks), and their coalescence into macrocracks [1-14]. The relationship between micro defects and ductile failure is firstly developed by McClintock [2]. After, three main approaches based on micro defects [15] are extensively used to describe the damage mechanics: fracture mechanics [3], micro-based damage mechanics [4, 16-18], and continuum damage mechanics. Since the limitations of first two methods, the continuum damage mechanics is more widely used in recent years. In CDM, the damage is assumed to be one of the internal state variables which relate to material behavior induced by the irreversible deterioration of microstructure. Lamaitre and Chaboche [6, 7] developed a fully coupled ductile damage model based on continuum damage mechanic. Tekkaya *et al.* [19] developed a fully coupled isotropic ductile damage constitutive model to predict the material behavior for metal blanking. Although these models have been applied for predicting the damage behavior, the damage evolution in complex loading histories has received little attention. The first aim in this paper is to develop an elasto-viscoplastic coupled multi-axial damage constitutive model based on Continuum Damage Mechanics (CDM) for blanking simulation. There are two aspects which are worth to mention:

- The isotropic ductile damage is coupled into a viscoplastic flow stress model based on the Continuum damage mechanics.
- A stress triaxiality-dependant and Lode angle-dependant stress state parameter is proposed into this constitutive model to control the damage evolution under the complex loading histories.

This fully coupled constitutive model has been implemented into a Dynamic Explicit Finite Element code (Abaqus/Explicit) using the user's subroutine. The local integration of the viscoplastic-damage

constitutive equations is performed using an asymptotic implicit scheme applied to only two scalar equations solved by Newton-Raphson algorithm.

Another challenge in sheet metal blanking is the problem of large plastic deformation, which makes the element severely distort during the finite element simulation. This problem can be solved by applying the adaptive meshing or remeshing scheme. Brokken [20] used the discrete fracture model and a 2D adaptive remeshing approach to simulate the sheet blanking process. And later, some other adaptive remeshing strategies [21, 22] for blanking were considered to avoid the element distortion in the blanking simulations in 2D. In this paper, an advanced 3D adaptive remeshing procedure is proposed. It is an important improvement of finite element method after its generation [23]. In this field, Borouchaki *et al.* [24-30] has made great contribution in both 2D and 3D. The adaptive remeshing scheme which he proposed had been widely used in elastoplastic-damage domain by Cherouat *et al.* [31]. It was also used in electromagnetic field by Borouchaki and Grosjes [29]. In this paper, a computing platform is constructed for integrating the 3D adaptive mesher OPTIFORM, the explicit solver and filed transfer (point to point) in order to simulate the sheet blanking process. The platform has the abilities to:

- Alleviate the computational costs: it adapts the finite mesh to the localized features so as to significantly improve the convergence rates and calculating accuracy of the finite element analysis.
- Reproduce the challenging feature: the crack propagation is well simulated by refining the element mesh size step by step and the element distortion in strain localization region is avoided.
- Remove the fully damaged elements during the metal blanking process.

The proposed numerical methodology is applied and validated into the tensile and compressive test. A sheet metal blanking model is constructed using proposed numerical methodology. Some technological parameters, including blanking clearance and tool wear are studied numerically based on this finite element model.

2. Constitutive model

2.1. *Elasto-viscoplastic fully coupled damage model*

To describe the gradual internal deterioration within the framework of continuum mechanics several continuum damage models, either phenomenological or micromechanically based, have been

developed. [Kachanov \[1\]](#) was the first to introduce the effective stress concept to model creep rupture. Isotropic damage formulations are extensively employed in the literature because of their simplicity, efficiency and adequacy for many practical applications. The constitutive equations for elasto-plasticity coupled with ductile damage adopted here have been originally proposed for small strains in the framework of irreversible processes with state variables by [\[6, 11, 21, 32-34\]](#). Yield function f is defined, according to the principle of strain equivalence, by:

$$f(\underline{\sigma}, R, D) = J_2(\underline{\sigma}) - R(\bar{\varepsilon}^p, \underline{\mathcal{E}}^e) - \sigma_y \quad (1)$$

where $J_2 = \sqrt{\frac{3}{2} \underline{S} : \underline{S}}$ is the second invariant of the stress tensor and $\underline{S} = \underline{\sigma} - \frac{1}{3} \text{tr}(\underline{\sigma}) \mathbf{1}$ is the deviatoric part of the Cauchy stress tensor, $R(\bar{\varepsilon}^p, \underline{\mathcal{E}}^e)$ is the isotropic hardening function and σ_y is the uniaxial yield stress of the virgin material.

The different effects of damage variable ($0 \leq D \leq 1$) on the effective modulus in tension and compression can be manipulated by the parameter h ($0 \leq h \leq 1$) which characterizes the effect of the closure of micro-cracks in a compression loading state. The value $h=1$ stands for the damage evolution in the tensile state without the crack closure effects, and $h=0$ corresponds that the crack is closed and there is no damage evolution within the pure compressive state. The value of h is often taken close to 0.2 which is typically observed in many experiments ([Besson, 1990](#), [Benzerga et al. 1990](#), [Lemaitre 1992](#), and [Lou 2017](#)). In order to perform the effect of this damage variable on the mechanical behavior, the effective state variables ($\underline{\mathcal{E}}^e$) are introduced:

$$\begin{cases} \langle \underline{\mathcal{E}}^e \rangle_+ = \frac{\langle \underline{\sigma} \rangle_+}{\sqrt{1-D}} & \langle \underline{\mathcal{E}}^e \rangle_- = \frac{\langle \underline{\sigma} \rangle_-}{\sqrt{1-hD}} \\ \langle \underline{\mathcal{E}}^e \rangle_+ = \langle \underline{\varepsilon}^e \rangle_+ \sqrt{1-D} & \langle \underline{\mathcal{E}}^e \rangle_- = \langle \underline{\varepsilon}^e \rangle_- \sqrt{1-hD} \end{cases} \quad (2)$$

where h is the stress state parameter used to determine the effect of the stress state on ductile material failure and it will be determined later. The positive part $\langle x \rangle_+$ considers the damage evolution for the elements that are in the tensile state. These parts accumulate the damage when the elements were in tensile stress state. The negative part $\langle x \rangle_-$ considers compressive state where the damage evolution is controlled by the parameter (h).

The stress-like variables, Cauchy stress tensor and scalar state variable associated with the isotropic ductile damage variable can be derived by Clausius-Duhem Inequality respectively:

$$\begin{cases} \underline{\sigma} = 2\mu_e(1-hD)\underline{\varepsilon}^e + \lambda_e(1-hD)(\underline{\varepsilon}^e : \underline{1})\underline{1} = \langle \underline{\sigma} \rangle_+ + \langle \underline{\sigma} \rangle_- \\ Y = h \left[\mu_e (\underline{\varepsilon}^e : \underline{\varepsilon}^e) + \frac{\lambda_e}{2} (\underline{\varepsilon}^e : \underline{1})^2 \right] = \langle Y_e \rangle_+ + \langle Y_e \rangle_- \end{cases} \quad (3)$$

where (λ_e, μ_e) are classical Lamé's constants,

$$\begin{cases} \langle \underline{\sigma} \rangle_+ = \lambda_e \langle \underline{\varepsilon}^e : \underline{1} \rangle_+ \langle \underline{1} \rangle_+ (1-D) + \mu_e \langle \underline{\varepsilon}^e \rangle_+ (1-D) \\ \langle \underline{\sigma} \rangle_- = \lambda_e \langle \underline{\varepsilon}^e : \underline{1} \rangle_- \langle \underline{1} \rangle_- (1-hD) + \mu_e \langle \underline{\varepsilon}^e \rangle_- (1-hD) \end{cases} \quad (4)$$

and

$$\begin{cases} \langle Y_e \rangle_+ = \frac{1}{2} \lambda_e \langle \underline{\varepsilon}^e : \underline{1} \rangle_+^2 + \frac{1}{2} \mu_e \langle \underline{\varepsilon}^e \rangle_+ : \langle \underline{\varepsilon}^e \rangle_+ \\ \langle Y_e \rangle_- = \frac{1}{2} h \lambda_e \langle \underline{\varepsilon}^e : \underline{1} \rangle_-^2 + \frac{1}{2} h \mu_e \langle \underline{\varepsilon}^e \rangle_- : \langle \underline{\varepsilon}^e \rangle_- \end{cases} \quad (5)$$

In the framework of CDM, the existence of a damage dissipation potential F_D is assumed and, in the case of plasticity damage, the total dissipation potential is given as,

$$F = f + F_D = f + \frac{1}{(\alpha+1)} \frac{\gamma}{(1-hD)^\beta} \left(\frac{Y - Y_0}{\gamma} \right)^{\alpha+1} \quad (6)$$

The parameters $(Y_0, \alpha, \beta$ and $\gamma)$ are damage parameters which can control the evolution of ductile damage shape and evolution. According to hypothesis of normality of the evolution of the plastic flow, the spatial modified plastic stretching tensor and the continuum damage variable are assumed to be governed by the equation:

$$\begin{cases} \underline{\mathcal{E}} = \mathcal{R} \frac{\partial F}{\partial \underline{\sigma}} = \frac{3}{2} \frac{\mathcal{R}}{\sqrt{1-hD}} \frac{S}{J_2(\underline{\sigma})} \\ \mathcal{D} = \mathcal{R} \frac{\partial F_D}{\partial Y} = \mathcal{R} \frac{1}{(1-hD)^\beta} \left(\frac{Y - Y_0}{\gamma} \right)^\alpha \end{cases} \quad (7)$$

For the isotropic hardening variable, the equivalent plastic strain rate is updated as:

$$\underline{\mathcal{E}}^e = \sqrt{\frac{2}{3} \underline{\mathcal{E}} : \underline{\mathcal{E}}} = \frac{\mathcal{R}}{\sqrt{1-hD}} \quad (8)$$

where \mathcal{R} is plastic multiplier determined by the consistency conditions:

$$\mathcal{R} = \frac{\partial f}{\partial \underline{\sigma}} : \underline{\mathcal{E}} + \frac{\partial f}{\partial R} \mathcal{R} + \frac{\partial f}{\partial D} \mathcal{D} = 0 \quad (9)$$

To be complete, one should give the non-symmetric fourth order tangent elastoplastic operator $\underline{\mathcal{L}} = \underline{L}_T : \underline{\mathcal{E}}$, where \underline{L}_T is defined as:

$$\underline{\underline{L}}_T = 2\mu_e (1-D) - 3\mu_e \frac{(1-D)}{H_p} \left(\frac{\underline{\underline{S}}}{J_2(\underline{\underline{\sigma}})} \otimes \frac{\underline{\underline{S}}}{J_2(\underline{\underline{\sigma}})} \right) - \frac{3\mu_e}{H_p (1-D)^{\beta+1/2}} \left(\frac{Y-Y_0}{\gamma} \right)^\alpha \left(\frac{\underline{\underline{S}}}{J_2(\underline{\underline{\sigma}})} \right) \otimes \underline{\underline{S}} \quad (10)$$

where H_p is the tangent plastic hardening module given by:

$$H_p = 3\mu_e + \frac{\partial R}{\partial \bar{\epsilon}^p} - \frac{h}{2\sqrt{1-hD}(1-hD)^{\beta+1}} \left(\frac{Y-Y_0}{\gamma} \right)^\alpha J_2(\underline{\underline{\sigma}}) \quad (11)$$

2.2. Visco-plastic hardening model

Viscoplasticity is usually modeled in three-dimensions using overstress models of the Perzyna or Duvaut-Lions types [35]. In these models, the stress is allowed to increase beyond the rate-independent yield surface upon application of a load and then allowed to relax back to the yield surface over time. The yield surface is usually assumed not to be rate-dependent in such models. An alternative approach is to add a strain rate-dependence to the yield stress and use the techniques of rate independent plasticity to calculate the response of a material [36].

The Johnson–Cook (JC) model [37] is purely empirical and the most widely used in thermo-mechanic field. Since the temperature effect is not important in the blanking process and the thermal effects are ignored. Johnson-Cook hardening is a particular type of isotropic hardening where the static yield stress, is assumed to be of the form:

$$\sigma_0(\bar{\epsilon}^p) = \left[A + B(\bar{\epsilon}^p)^n \right] \quad (12)$$

where (A, B and n) represent the isotropic hardening evolution

The Johnson-Cook strain rate dependence assumes that:

$$R(\bar{\epsilon}^p, \dot{\bar{\epsilon}}^p) = \sigma_0(\bar{\epsilon}^p) \left[1 + C \ln \frac{\dot{\bar{\epsilon}}^p}{\dot{\bar{\epsilon}}_0^p} \right] \quad (13)$$

where $\dot{\bar{\epsilon}}^p$ is the equivalent plastic strain rate, $\dot{\bar{\epsilon}}_0^p$ is the initial strain rate determined experimentally and C represent the material viscosity parameter.

2.3. Stress state parameter

The multi-axial damage evolution is necessary in blanking simulation. For instance, the surface of workpiece which is contacted with the punch undergoes compressive stress state. If there is no configuration of multi-axial damage evolution, the damage in these compressive regions will

accumulate faster than that in others where undergo tensile or shearing stress state. This will lead to the rapid degradation of the material stiffness in the compressive region and it is not practical.

Theoretically speaking, the damage caused by the microdefects has different evolution processes when the state of stress changes. The micro-defects can open in the tensile state will close in compressive state. Some quasi-unilateral model [38, 39] is developed to consider this recovery effect of physical properties after closure of microdefects. This paper proposes a multi-axial damage evolution model through defining a stress state parameter $h(\xi, \theta)$ which is associated with stress triaxiality (ξ) and Lode angle (θ).

The stress state should be defined to confirm the stress state parameter. At an isotropic material point we can described the stress state by three invariants:

$$J_1 = \frac{1}{3} \text{tr}(\underline{\sigma}), \quad J_2 = \sqrt{\frac{3}{2} \underline{S} : \underline{S}}, \quad \text{and} \quad J_3 = \left(\frac{27}{2} \det \mathbf{S} \right)^{\frac{1}{3}} \quad (14)$$

The invariant J_1 represents the hydrostatic component of the current stress state; J_2 and J_3 represent the second and third stress invariants measure of the deviatoric stress tensor. It is convenient to work with the dimensionless hydrostatic pressure defined by:

$$\xi = \frac{J_1}{J_2} \quad (15)$$

The second important parameter is the Lode angle θ_0 which is related to the normalized third deviatoric stress invariant χ , can be written as:

$$\chi = \left(\frac{J_3}{J_2} \right)^3 = \cos(3\theta_0) \quad (16)$$

The Lode angle has the range of $0^\circ \leq \theta_0 \leq 60^\circ$ is an indication of the magnitude of the intermediate principal stress in relation to the minor and major principal stresses. The normalized third deviatoric stress invariant χ has the range of $-1 \leq \chi \leq 1$. For calculation purposes, θ_0 is also normalized by:

$$\theta = 1 - \frac{6\theta_0}{\pi} = 1 - \frac{2}{\pi} \arccos \chi \quad (17)$$

which can make the Lode angle have the normalized range of $-1 \leq \theta \leq 1$. This normalized will be called the Lode angle parameter hereinafter. The stress state parameter $h(\xi, \theta)$ can be calculated when stress triaxiality and Lode angle confirmed as:

- **First step** : is to fit respectively three main controlling curves which only consider the stress triaxiality using a same simple logistic-growth expression, as follows:

$$h(\xi) = \frac{1}{1 + ae^{-b\xi}} \quad (18)$$

The logistic-growth function is used to describe the growth of a lower limit 0 and an upper limit 1, which fits the stress state parameter property. Parameters a and b are material constants, which have the ability to control the start value or end value of $h(\xi)$ and shape of the curves in a certain interval of ξ . For metal forming and machining, the hydrostatic loading for the material point undergoes a hydrostatic loading mostly in the interval of $(-1 \leq \xi \leq 1)$ and we also focus on studying the material damage behaviour in this interval.

Three different stress state parameter curves $h(\xi)$ in tension, shear and compression are fitted respectively by different sets of material parameter (a, b), as shown in Fig. 1. Comparing these three curves, we can find that the stress state parameter curve in tension dominates the damage evolution when ξ is greater than 0.4; and the stress state parameter curve in shear replaces that in tension when ξ is smaller than 0.4. One can also observe that the stress state parameter is near to zero when ξ is smaller than $-1/3$ in the stress state parameter curve in tension, which leads to a very slow accumulation of damage energy. However, the stress state parameter in shear is keeping a high level even in the negative stress triaxiality state. Actually, there are some differences for different metals in the transition range, which ξ is in the interval of $(0 \leq \xi \leq 0.4)$. The value of $\xi = 0.4$ can be called the transition point. The transition point can be changed in different metals and two different types of metal may be classified using the value of transition point. The curve increases with the stress triaxiality for materials having smaller equivalent strain to fracture in shear, such as steel 4340, aluminium Al2024-T351, while the curve decreases with the stress triaxiality for materials having larger equivalent strain to fracture in shear, such as aluminium 1100-0 and copper OFHC (Bao and Wierzbicki 2005).

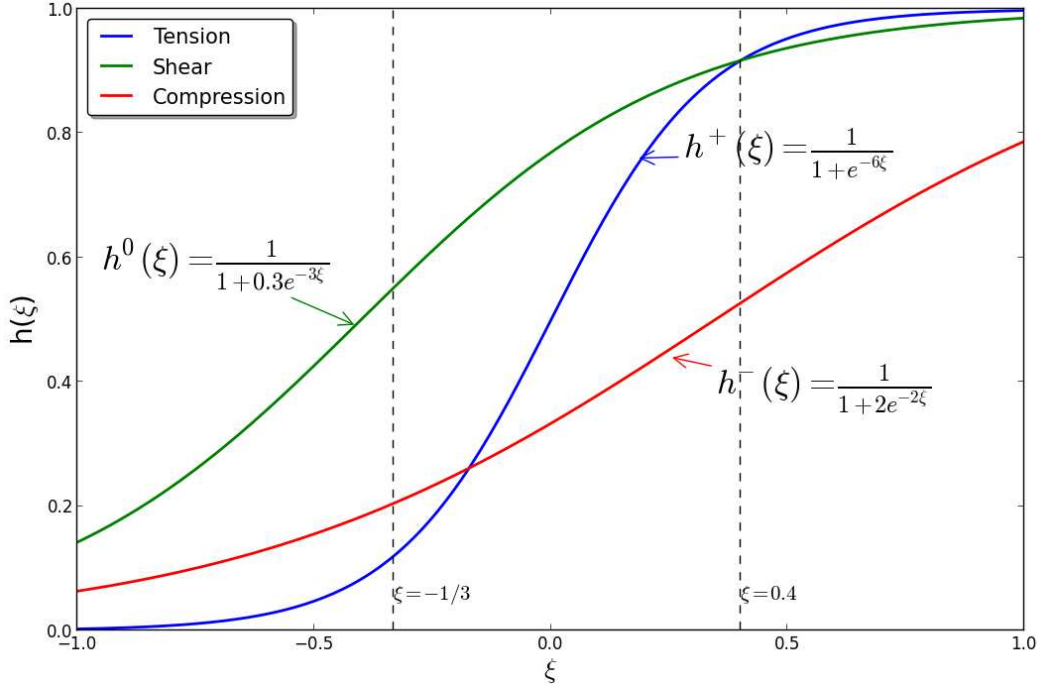


Figure 1. Three principal stress state curves of tension, shear and compression

- **Second step:** is to introduce the effect of the Lode angle. Three stress state parameter curves associated with stress triaxiality are presented respectively for tensile state $h^+(\xi)$, shear state $h^0(\xi)$ and compressive state $h^-(\xi)$. Then the dependence on the Lode angle parameter θ is taken to be parabolic form, which can be written as:

$$h(\xi, \theta) = \left\{ \frac{1}{2} [h^+(\xi) + h^-(\xi)] - h^0(\xi) \right\} \theta^2 + \frac{1}{2} [h^+(\xi) - h^-(\xi)] \theta + h^0(\xi) \quad (19)$$

In the function of stress state parameter, six material constants needed to determine. Note that the main controlling curve $h^+(\xi)$ is corresponding to the bounding curve when $\theta=1$, $h^0(\xi)$ corresponds to the bounding curve when $\theta=0$ and $h^-(\xi)$ corresponds to the bounding curve when $\theta=-1$. The stress state parameter varies from 0 to 1, which stands for the changing of the stress state from compression, to compression-shear, to shear, to shear-tension and to tension. In various loading conditions, the symmetric stress state ($h^+ = h^0 = h^-$) the stress state parameter surface have weak effects of stress triaxiality and Lode angle. Strong effects of stress triaxiality and Lode angle are considered when different stress triaxiality bounding curves in tension, shear and compression are respectively adopted, as shown in Fig. 2. We observe that the stress state parameter in various loading conditions (ξ, θ) can be found in this surface. This strongly dependent stress state parameter surface

is coupled into our proposed constitutive equations in this work to study the damage evolution in complex loading conditions.

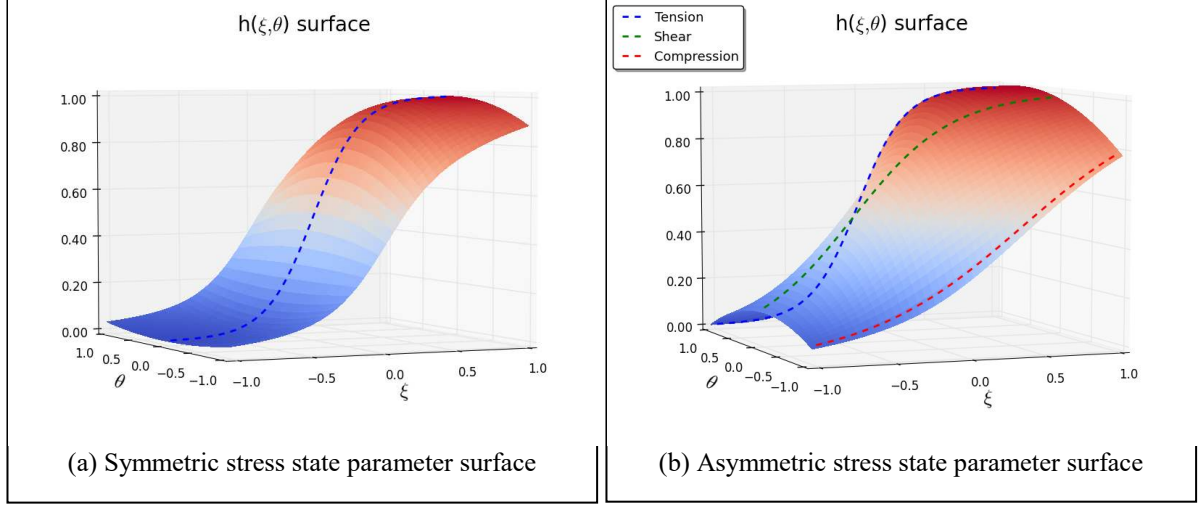


Figure 2. Stress state parameter surface with different stress triaxiality and Lode angle

2.4. Aspects of the numerical integration of constitutive equations

The finite element formulation of the large strain elastic-visco-plastic model coupled with damage follows standard updated Lagrangian formulation procedure, whereby equilibrium is expressed with respect to the current configuration:

$$G(\delta \mathbf{u}, \delta \mathbf{u}) = \int_V \rho \delta \mathbf{u} \cdot \delta \dot{\mathbf{u}} dV - \int_V \underline{\underline{\sigma}} : \delta \underline{\underline{\epsilon}} dV + \int_V \mathbf{f}_v \cdot \delta \mathbf{u} dV + \int_{\Gamma_\sigma} \mathbf{t} \cdot \delta \mathbf{u} d\Gamma + \int_{\Gamma_c} \mathbf{t}_c \cdot \delta \mathbf{u}_c d\Gamma \quad (20)$$

with $(\Gamma_u, \Gamma_\sigma, \Gamma_c)$, are parts of the boundary where the displacement vector, the force surface vector \mathbf{t} and the contact force surface vector \mathbf{t}_c are prescribed with $(\Gamma = \Gamma_u \cup \Gamma_\sigma \cup \Gamma_c)$. The vector \mathbf{f}_v is the body force field, while $\delta \mathbf{u}$ and $\delta \dot{\mathbf{u}}$ are the virtual kinematical admissible velocity and acceleration fields respectively and $\delta \mathbf{u}_c$ is the virtual velocity vector of contact nodes.

The integration of the rate evolution equations is accomplished by a radial return mapping algorithm, based on a dynamic explicit procedure. Explicit dynamic procedure performs a large number of small time increments efficiently. It is based upon the implementation of an explicit integration rule together with the use of diagonal (“lumped”) element mass matrices. The equations of motion for the body are integrated using the explicit central-difference integration rule:

$$\begin{cases} \mathbf{u}_{(i)}^N = (M^{NJ})^{-1} (P_{(i)}^J - I_{(i)}^J) \\ \mathbf{u}_{(i+1/2)}^N = \mathbf{u}_{(i-1/2)}^N + \frac{\Delta t_{(i+1)} + \Delta t_{(i)}}{2} \dot{\mathbf{u}}_{(i)}^N \\ \mathbf{u}_{(i+1)}^N = \mathbf{u}_{(i)}^N + \Delta t_{(i+1)} \dot{\mathbf{u}}_{(i+1/2)}^N \end{cases} \quad (21)$$

Where M^{NJ} is the mass matrix, P^j is the applied load vector, and I^j is the internal force vector. The degrees of freedom u^N in subscript i increment compute, $(n-1/2)$ and $(n+1/2)$ refer to middle increment values. Each increment is relatively inexpensive (compared to the direct-integration dynamic analysis procedure available in Abaqus/Standard) because there is no solution for a set of simultaneous equations. The material removing processes are the highly non-linear problems which includes material elastic-visco-plastic-damage behavior, complex boundary contact and geometric deformation. ABAQUS/Explicit solver is the first chose for us to solve the problems. The local integration of the fully coupled constitutive equations, implemented in ABAQUS/Explicit FE code using the user defined subroutine VUMAT, is performed using the return mapping algorithms together with the Euler implicit scheme based on the well-known elastic prediction/plastic correction as:

(i) Elastic predictor:

$$\sigma_{n+1}^{trial} = 2\mu_e (1 - h_n D_n) \underline{\varepsilon}_{n+1}^{trial} + \lambda_e (1 - h_n D_n) (\underline{\varepsilon}_{n+1}^{trial} : \underline{1}) \underline{1} \quad (22)$$

(ii) Check plastic consistency condition:

$$\text{If } f = J_2(\sigma_{n+1}^{trial}) - R(\bar{\varepsilon}_n^p, \underline{\varepsilon}_n^p) - \sigma_y \leq 0 \text{ THEN}$$

$$\text{Set } (\bullet)_{n+1} = (\bullet)_{n+1}^{trial} \text{ and RETURN}$$

ELSE go to (iii)

(iii) Visco-plastic corrector (solve simultaneously at each Newton-Raphson iteration the two unknowns system for $(\Delta\lambda_{n+1}, D_{n+1})$):

$$\begin{cases} f_1(\Delta D_{n+1}, \Delta\lambda_{n+1}) = \frac{J_2(\sigma_{n+1}^{trial})}{\sqrt{1 - h_n D_{n+1}}} - \frac{3G\Delta\lambda_{n+1}}{\sqrt{1 - h_n D_{n+1}}} - R(\bar{\varepsilon}_n^p, \underline{\varepsilon}_n^p) - \sigma_y = 0 \\ f_2(\Delta D_{n+1}, \Delta\lambda_{n+1}) = \Delta D_{n+1} + \frac{\Delta\lambda_{n+1}}{(1 - h_n D_{n+1})^\beta} \left(\frac{Y_n - Y_0}{\gamma} \right)^\alpha = 0 \end{cases} \quad (23)$$

(iv) Update

$$\left\{ \begin{array}{l}
\Delta \underline{\varepsilon}_{n+1}^p = \frac{\Delta \lambda_{n+1}}{\sqrt{1-h_{n+1}\Delta D_{n+1}}} \underline{n}_{n+1} \\
\bar{\varepsilon}_{n+1}^p = \bar{\varepsilon}_n^p + \frac{\Delta \lambda_{n+1}}{\sqrt{1-h_{n+1}\Delta D_{n+1}}} \\
\underline{\varepsilon}_{n+1}^e = \frac{1}{\Delta t} \frac{\Delta \lambda_{n+1}}{\sqrt{1-h_{n+1}\Delta D_{n+1}}} \\
\underline{\sigma}_{n+1} = \underline{\sigma}_n + [1-h_{i+1}\Delta D_{i+1}] \left[\lambda_e tr(\Delta \underline{\varepsilon}_{n+1} - \Delta \underline{\varepsilon}_{n+1}^p) + 2\mu_e (\Delta \underline{\varepsilon}_{n+1} - \Delta \underline{\varepsilon}_{n+1}^p) \right] \\
R_{n+1} = \left[A + B (\bar{\varepsilon}_{n+1}^p)^n \right] \left[1 + C \ln \frac{\underline{\varepsilon}_{n+1}^e}{\underline{\varepsilon}_0} \right]
\end{array} \right. \quad (24)$$

(v) RETURN

The Cauchy stresses are updated using elastic strain tensors; the stress triaxiality and Lode angle are calculated to update the new stress state parameter. During the whole process, the damage variable D accumulates from elastic stage to plastic stage until to the final fracture when D is greater than D_c at a given integration point. The correspondent elastic modulus will set to zero giving zero and element lost its capacity of loading when the fully damage reaches.

3.2. Adaptive remeshing procedure

The FEM based numerical simulation of sheet or bulk metal forming processes involving large irreversible deformations requires adequate spatial mesh discretization of the deformed domain. According to the large amount of plastic deformation undergone during sheet metal blanking, the initial mesh is highly distorted; frequent remeshing is needed during the computation in order to avoid mesh quality and also to control the errors caused by the approximation of the thermo-mechanical fields [49-52]. Two kinds of error estimates are proposed. The first deals with the gradient of the damage field (physical error estimation) and the second, concerns the local curvature of both the formed part and the forming tools (geometrical error estimation).

This allows to adapt the mesh in order to improve the damage localization leading to a macroscopic crack; and to improve the non-penetration condition concerning the contact boundary between the damaged part and the tools. To mesh the computational domain, we consider a combined approach which uses a frontal method to define field points and Delaunay method to construct the connection between these points. This remeshing technique is extended to the case where a prescribed size map is given, for example by means of an *a posteriori* error estimate (damage or plastic strain). In this case we consider the intersection of the geometric map and the prescribed size map to govern the remeshing of the domain. An adaptive remeshing computing platform is implemented using Python

script and it integrates the 3D adaptive mesher, the ABAQUS/Explicit solver and the field transfer (point to point). The Python script divides the actual loads into numerous sub-loads and implements the load Δu step by step.

1. At the first iteration, the initial geometrical domain Ω and its boundary $G_1(\Gamma)$ are necessary to give out using the spatial discretization based on tetrahedral finite elements. The solution $S_0(\Omega)$ on the Gauss points of these elements also needs to be specified if they exist as the initial conditions.
2. The final deformation is assumed to be obtained iteratively, after several "small" loading steps (which is the case in the framework of an explicit integration scheme for solving the problem). At the following load step, the meshes are refined or coarsened automatically according to the constantly changing physical fields and geometrical shape; the element qualities are evaluated and optimized to the regular or similar regular tetrahedral elements; and the physical fields are transferred (point to point) from the old mesh to the new one using advanced algorithm.
3. The fully damaged elements are deleted when the damage field D greater than D_{\max} and the new boundaries can be redefined in this process. The damage field is also a reference to refine the mesh in domain Ω , and the mesh size is imposed to reach the smallest value if the damage field greater than the critical value D_c .

The proposed adaptive remeshing procedure is a numerical calculating environment integrates explicit solver, OPTIFORM adaptive mesher and point to point field transfer algorithm. It is based on tetrahedral elements and updates the mesh step by step automatically. During the procedure, both prior and posteriori error estimates are used to refine the mesh; the temperature-displacement dynamic explicit in ABAQUS is chosen to solve metal forming processes; the physical field in nodes (temperature) and element interpolation points (stress, equivalent plastic strain and damage variable) are transferred.

3.1. Remeshing procedure

OPRIFORM mesher can provide us the adaptive mesh of tetrahedral finite elements. The unit remeshing strategy and Constraint Delaunay kernel are proposed to refine and coarsen automatically the FE meshes. It uses edge removing and edge-based refinement combined with a constraint Delaunay method to construct a unit mesh. Hence, the FE mesh optimize from both element and its edges. Prior and posterior error estimates are interpolated to generate different mesh size map and control the local mesh density. The elements will be killed in OPTIFORM when damage criterion is

satisfied. The new boundary is constructed after unit mesh generating, edges/elements optimizing and elements killing. The field both on nodes and elements are transferred. Fields on element, such as stress and plastic strain, are transferred through Gauss point from old mesh to the new one. Fields on node, such as temperature, is transferred based on fast point and element search algorithm [] from old mesh to the new one directly.

Based on above function, the adaptive remeshing procedure (see Fig. 3) used in metal forming processes can be described as: we consider Ω_1 and Ω_2 as the initial domain of work-piece and cutter/punch respectively in R^3 ,

1. Computation the finite element model created by Ω_1 and Ω_2 . Solution S at each step time is defined for Ω_1 ;
2. Detection of contact region and deformation zone using prior error estimate. The first mesh size map H_{geo} will be defined as a prior metric field to govern the remeshing domain;
3. Confirmation of local mesh quality using posterior error estimation based on physical field solution S . The second mesh size map H_{phy} (include damaged) will be defined as a posterior metric field to govern the remeshing domain;
4. Intersection of the mesh size map and definition the unique size map to adaptive remesh and optimize the domain; the new boundary Ω_1' and Ω_2' are created.
5. Transfer of thermal-mechanical fields from Ω_1, Ω_2 to Ω_1', Ω_2' ; return to step 1.

The above cyclic process divides the whole metal forming process into several iterations and the adaptive remeshing procedure is implemented at each iteration to ensure mesh qualities. During each adaptive remeshing iteration, the mesh size is controlled by element minimal size H_{min} and maximum size H_{max} . The contact region is detected and remeshed based on prior estimate. The mesh is optimized and refined based posterior estimate which can be chosen in provided physical solution S , for example equivalent plastic strain. The field of damage must be calculated through various damage criterions and the damaged elements are killed according to the given field. The finite element simulation for metal forming processes will be finished when all of these iterations are implemented successfully.

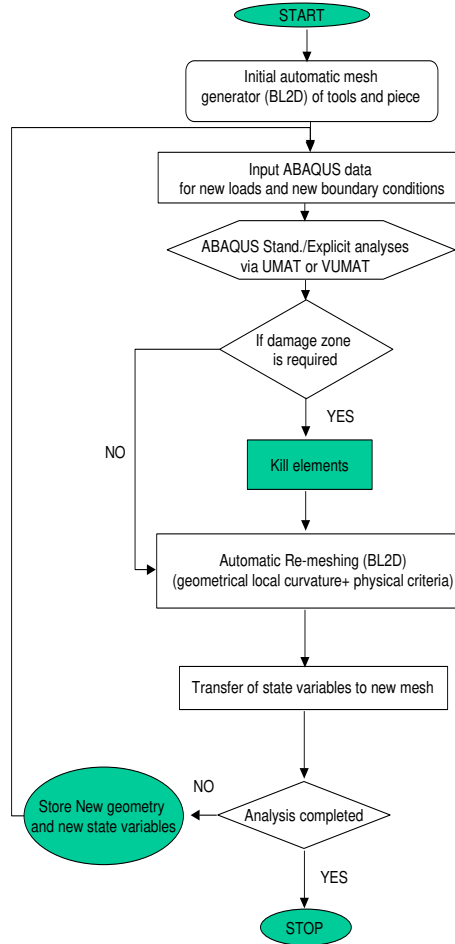


Figure 3. Flowchart of the used shell Script

3.2. Error estimation

The local mesh density is governed by an element size map which is consistent with the underlying geometry of the deformed domain and the improvement of the accuracy of the desired mechanical fields. Metal forming, such as metal orthogonal cutting and blanking are complex contact and deformation or damage problems. To obtain an accurate FE simulation for metal forming, the mesh of local contact and deformation region must refine firstly. The zone which includes a kind of physical field with high gradient distributions must be refined secondly. Simultaneously, the unconcerned regions should be keeping coarse to save computing cost. In this paper, both priori and posterior estimate was used to reach these purpose.

- A priori error estimate was presented to identify the nodes and elements of the part which contact with tools. As master contact surface, tool's surface and its normal need to be given out before remeshing. The priori remeshing region $R_\delta(s)$ which associates with the surface s is defined by:

$$R_\delta(s) = \{X \in R^3, d(N, s) \leq \delta\} \quad (25)$$

Where $d(N, \hat{n})$ is the distance between node N and \hat{n} through the normal direction from tool's surface to part's surface, and δ is detect displacement which needs to be defined initially. The first geometrical size map generates and stores when priori error estimate is defined as (Fig. 4):

$$\begin{cases} H_{\text{geo}} = 2\rho \sin(\beta) & \text{Angular} \\ H_{\text{geo}} = 2\sqrt{\delta(2\rho - \delta)} & \text{Curvature} \end{cases} \quad (26)$$

- A posteriori error estimator depending on the given field solution interpolates the error and optimizes the finite mesh again. The mesh size of the whole region has a gradient refinement according to the given solution. The region which is attributed with the higher field solution than the give threshold K_{crit} will be refined to H_{min} . This procedure always implements in lots of small deformed iterations to avoiding element distorting and ensure calculating accurately.

In this paper, the equivalent plastic strain $\bar{\epsilon}^p$ is chosen to control the mesh size adaptively :

$$\begin{cases} \text{if } (\bar{\epsilon}^p < K_{\text{crit}}) & H_{\text{phy}} = h_{\text{max}} + (H_{\text{min}} - H_{\text{max}}) \left(\frac{\bar{\epsilon}^p}{K_{\text{crit}}} \right)^\alpha \\ \text{Else} & H_{\text{phy}} = H_{\text{min}} \end{cases} \quad 0 < \alpha \leq 0.7 \quad (27)$$

- The damage field is also considered to kill the fully failed elements. The mesh with the new boundary generates after elements killing. Mesh damage size H_D to the damage

$$\begin{cases} H_D = H_{\text{max}} & 0 \leq D < D_c \\ H_D = h_{\text{max}} + (H_{\text{min}} - H_{\text{max}}) e^{\kappa \ln(\frac{D}{D_{\text{max}}})} & D_c \leq D < D_{\text{max}} \\ H_D = H_{\text{min}} & D = D_{\text{max}} \end{cases} \quad 0 < \kappa \leq 0.5 \quad (28)$$

- The intersection of the geometric map and the prescribed size map govern the remeshing of the domain is defined as :

$$H = \text{Min}(H_{\text{geo}}, H_{\text{phy}}, H_D) \quad (29)$$

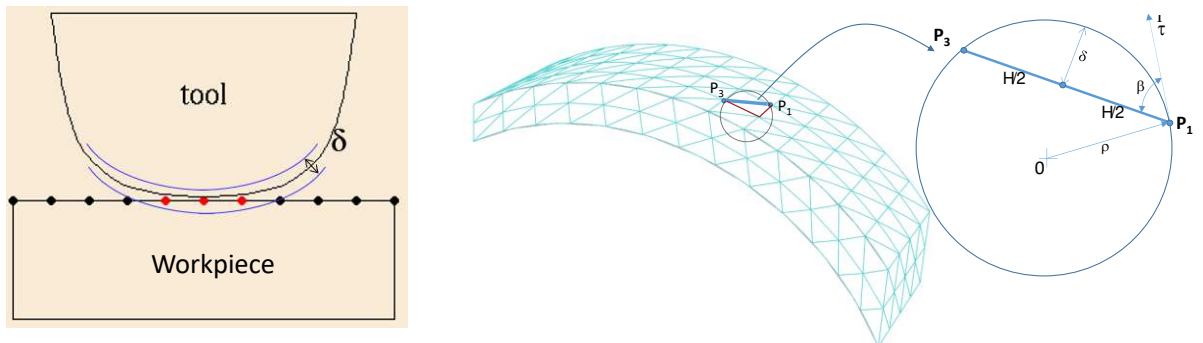


Figure 4. Geometrical mesh size

3.3. Transfer, consistent recovery and equilibrium

The generation of a new mesh in the remeshing process, the state variables from the old mesh must be transferred to the new mesh. One can either completely recompute the simulation variables or transfer the variables from the old mesh to the new mesh.

Two groups of transferal techniques:

- techniques to transfer discontinuous variables which are continuous within each element and stored at Gauss points such as stress, state variable and damage ;
- techniques to transfer continuous variables stored at nodes such as displacement, velocity and temperature.

The variables at the Gauss points of the new mesh are obtained from the nodal points using shape functions. After generating the new mesh, the thermo-mechanical fields should be transferred from the old mesh to the new one, such that the computation may continue without excessive error. To achieve this successfully, two main methods are usually used, namely the standard interpolation and the projection techniques. However, for problems with high physical (finite elastic-visco-plasticity, damage, friction, ...) and geometrical (evolving contact, large transformation, ...) nonlinearities, some improvements should be made. In fact, on the old mesh the concerned fields verify (in the FE sense) both the global equilibrium equations (displacement and temperature fields at nodes) as well as the constitutive equations (stress and internal variable fields at integration points).

Accordingly, the transfer operation, which should address the following issues:

- (1) the verification of the static equilibrium equations (static admissibility);
- (2) consistency with constitutive equations (plastic admissibility);
- (3) compatibility with the displacement or velocity fields on the new mesh (kinematic admissibility);
- (4) compatibility with evolving boundary conditions (unilateral contact conditions) and with the rupture condition (critical value of damage);
- (5) minimization of numerical 'diffusion' of state variables.

5. Application to metal forming

Blanking is a metal stamping operation by which the sheet metal is punched to get the required outer profile of the sheet metal component. During the blanking process the punch tool penetrates into the sheet metal and forces the material into the die. A small clearance exists between the punch and die

tools. When the punch impacts the sheet, the metal in this clearance quickly bends and then fractures. The blank which has been sheared from the large piece of sheet metal now falls freely into the gap in the die. This process is extremely fast, with some blanking presses capable of performing over 1000 strokes per minute. The effects of shearing on the material change as the cut progresses and are visible on the edge of the sheared material. When the punch impacts the sheet, the clearance between the tools allows the sheet to plastically deform and generates a depth of rollover at the sheared edge. The part of the material is pushed by the punch in this stage. Following with the further penetration, the shear force leads to a vertical burnished zone of material. Finally, the shear stress is too great and the material fractures at an angle with a small burr formed at the edge.

In this work, 3D sheet metal forming examples will be now presented in order to test the capability of the proposed numerical methodology to predict the ductile damage occurrence during the cutting process as well as its ability to study the influence of the process technological parameters on the sheet quality. All presented results herein are obtained with the fully isotropic model concerning elasticity, plasticity and damage.

5.1. Tensile test of OFHC copper alloy

The first example investigates the material plastic properties required to completely blanking operation and the second example investigates the effect numerical and blanking parameters on the predicting of ductile damage during the cutting process.

Properties of the used oxygen-free-high-conductivity OFHC copper alloy obtained from the tensile tests, are given in [Table 1](#). With these parameters and the absence of experimental information about the softening stage due to the damage effect as well as the precise experimental value of the ductility, the damage coefficients have been estimated in order to have a maximum effective stress of $\bar{\sigma}_{\max} = 383\text{MPa}$, the plastic strain at damage initiation $\varepsilon_p = 0.22$ and the plastic strain to fracture $\varepsilon_f = 0.26$. The fully coupled predicted true effective stress-true plastic strain curve for both uncoupled and fully coupled cases obtained in simple tension is given is compared to the experimental values in [Fig. 5](#). The damage evolves from the damage initiation to the fracture and the material stiffness degrades from maximum tensile force to zero.

The tensile tests are simulated firstly without remeshing for both coupled and uncoupled cases. In the case of a calculation without remeshing, 3D continuum hexahedral finite elements are used and a fine mesh ($H = 0.01\text{mm}$ in the region of localization) are applied to simulate the localization of the equivalent plastic strain and also the ductile damage. The iso-values of the damage in the specimens with/without remeshing procedure are shown in [Fig. 6](#).

The localization phenomenon of damage, the formation of a crack and its propagation to the final fracture were accurately simulated. Firstly, the damage focused in the centre of the specimen and the shear band extended from centre to the two sides along the direction of a 45°. Then, the crack generates in the center at a displacement of $U=1.0\text{mm}$ and propagates along the shear band when the tensile displacement increased from $U=1.586\text{mm}$ to $U=1.587\text{mm}$. Finally, the specimen fractured when the tensile displacement move from $U=1.587\text{mm}$ to $U=1.588\text{mm}$ (see Fig. 6).

In the case of fully coupled model with damage without remeshing (Fig. 6b), the damage localization appears in the middle at a displacement of $U=0.5\text{mm}$. And then, two shear bands are formed quickly at a displacement of $U=1.24\text{mm}$. The damage variable reaches to the maximum value $D=1$ in the cracked zones at a displacement of $U=1.5\text{mm}$. However, in the uncoupled case (Fig. 6a), the damage variable is invalid and there is no damage localization exists. The simulation results also have shown us that the crack generation and propagation can be well simulated with the help of adaptive remeshing scheme. The adaptive remeshing scheme constantly refines the mesh size according to the damage accumulation and optimizes the element quality after large deformation. This is helpful to simulate some problems when damage and crack formation exist.

Table 1. Elastic-visco-plastic parameters of the OFHC copper

E (GPa)	ν	A (MPa)	B (MPa)	n	C	Y_0	α	β	γ	h	$\frac{\sigma_0}{E}$
124	0.34	90	280	0.45	0.025	0.38	0.2	0.3	0.37	0.2	1%

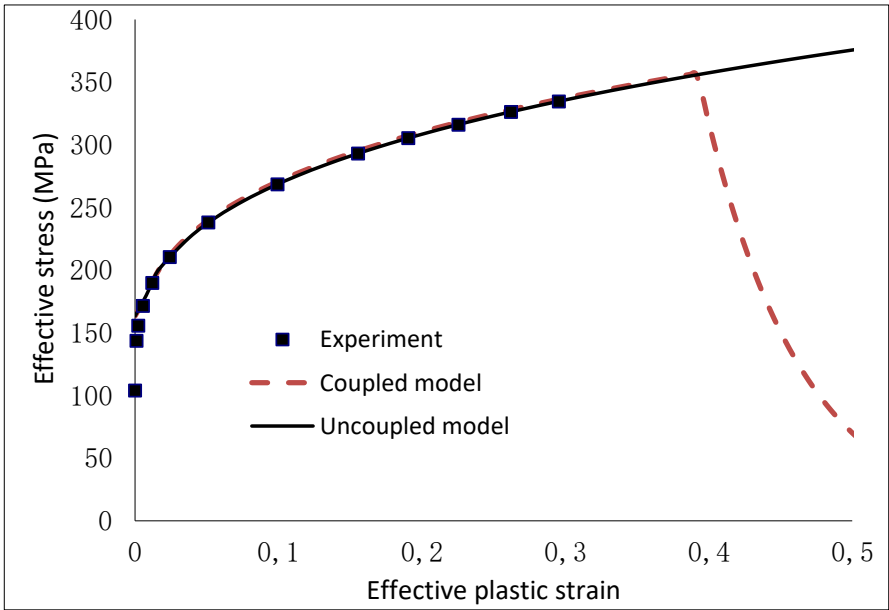


Figure 5. Predicted stress-strain curve of OFHC copper material

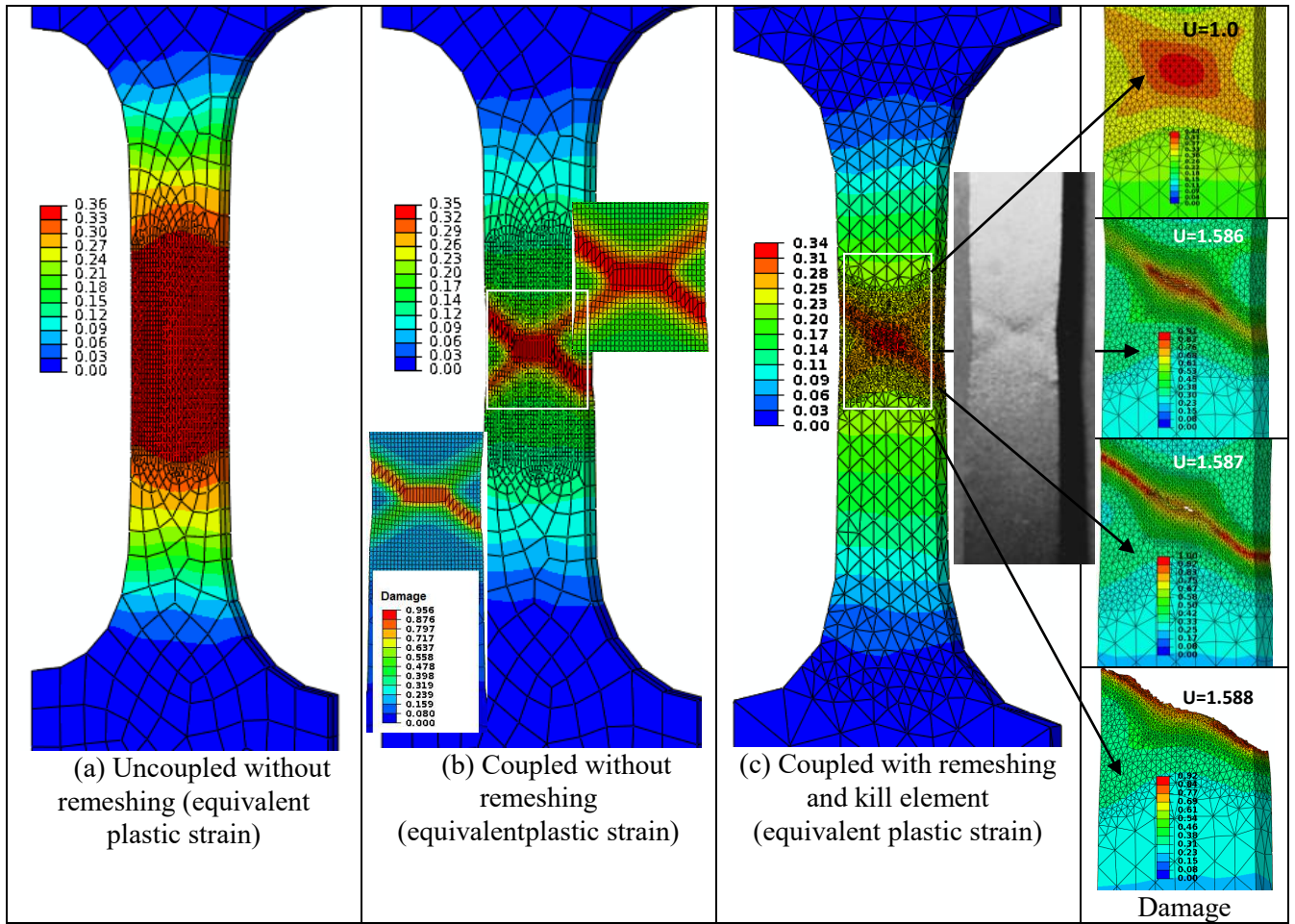


Figure 6. Ductile damage localization in various case

In Figure 7, the predicted force-displacement curves with and without remeshing are compared with the experiment values. From this figure, one can observe the simulation results fit well the experiment values in the plastic stage and the effect of the damage-induced softening are clearly in the simulation using fully coupled damage constitutive equations. These results prove that the proposed numerical methodology using elastoplastic fully coupled ductile damage model and adaptive remeshing procedure is reliable to predict the material behavior.

Three minimum mesh size $H_{\min}=0.5\text{mm}$ (coarse), $H_{\min}=0.1\text{mm}$ (moderate coarse) and $H_{\min}=0.05\text{mm}$ (fine) were used to study the sensibility of mesh size on the tensile force-displacement curves (see Fig. 8). It is clear that the damage evolution is sensitive to the element size and the damage variable accumulates more quickly in the smaller mesh size simulation. Some future works will be concentrated in solving the mesh size effect.

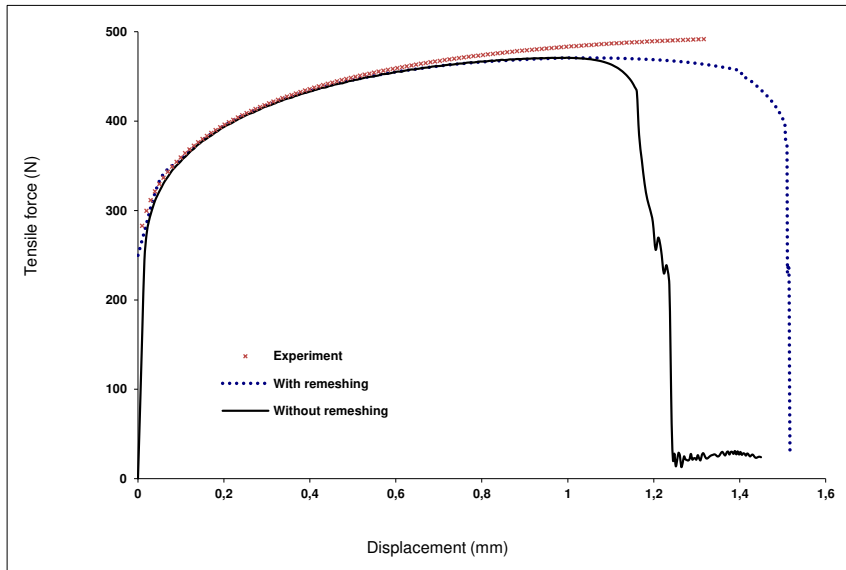


Figure 7. Tensile force versus displacement of OFHC copper material

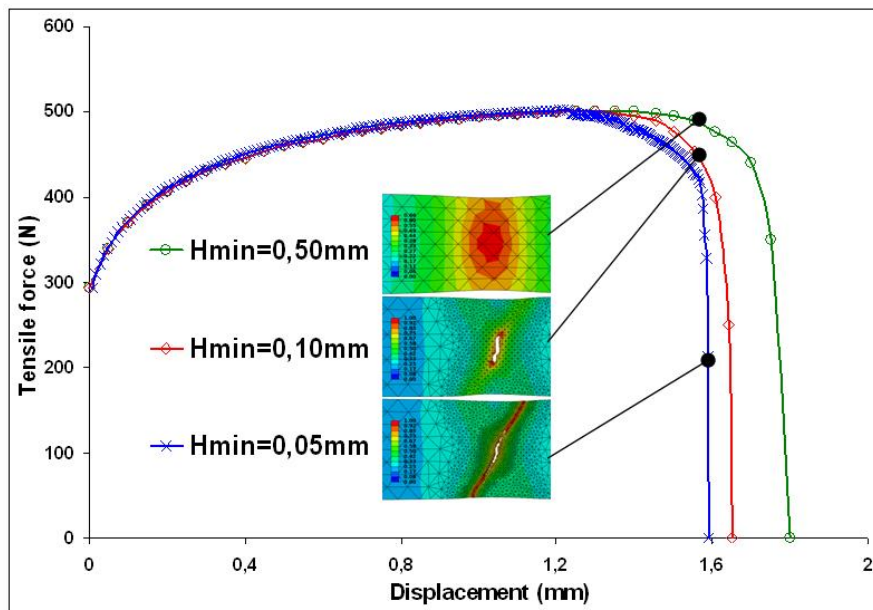


Figure 8. Mesh size effect on the response of tensile force-displacement

5.2. Application to sheet metal blanking

The main purpose of the numerical simulation is to “virtually” predict a final sheared edge free from any defect (ratio of burnished edge, burr height), to estimate the residual stress profile through the thickness and the maximum blanking force versus displacement [52-66]. The geometrical model (Table 2) and the boundary conditions of cylindrical sheet metal blanking are described in Fig 9. The numerical model will be validated through comparing the blanking force and the profiles of sheared edge with the experimental results [46, 51].

Table 2. Geometrical parameters of sheet blanking

v (mm/s)	t (mm)	c (μm)	$\text{\O}D_p$ (mm)	$\text{\O}D_d$ (mm)	R = r (μm)
20	0.58	15	3.5	3.53	10

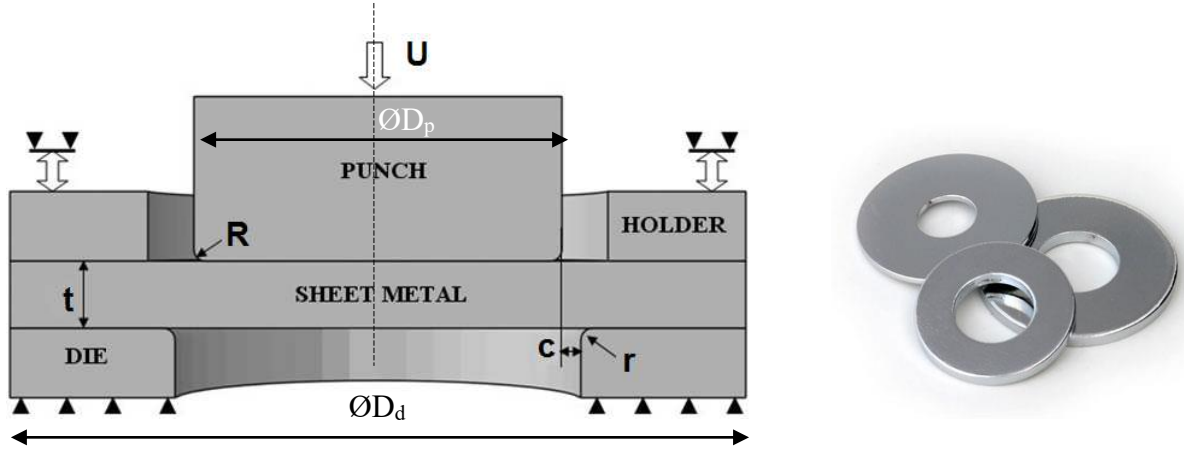


Figure 8. Geometry parameters and boundary conditions of blanking process

Because of the symmetry of the problem, only the quarter of the circular disc is modelled. The sheet is discretized initially by 1284 linear tetrahedral elements (C3D4 tetrahedral elements in ABAQUS element library). The appropriate symmetry conditions are applied at the axis of symmetry. The punch, die and blank-holder tools are modeled by quadrilateral rigid elements. The friction coefficient ($\mu = 0.1$) is used in both surface to surface contact (punch/die and work-piece) and self-contact (fractured surface). The punch force is generated by a constant velocity of 20mm/s. The mass scaling is used for computational efficiency: the first fixed mass scaling definition scales the masses in the entire model by a factor (100); the second fixed mass scaling definition together with the first definition by scaling the masses of any elements whose stable time increments are less than 1×10^{-7} .

The first mesh was mainly controlled by geometrical error estimate, which means that the element size in the range of detected distance between part and tools (Hausdorff distance δ) were refined to small size H_{\min} at the beginning of simulation. The refined mesh based on both geometrical and physical error estimates were focused on the contact region between the sheet and tools, where forecasts of existing large plastic deformation and fracture (see Table 3). At each punch penetration, the element size is adapted to equivalent plastic strain and element killing accords to the fully damage variable.

Table 3. Adaptive remeshing parameters for the blanking of the OFHC sheet

H_{\min}	H_{\max}	Critical damage Dc	Damage max D_{\max}	Hausdorff distance δ
0.01 mm	0.5 mm	0.5	0.9999	0.02 mm

The deformed meshes and damage distributions in sheet are plotted in Fig. 9 for each punch displacement. At each penetration of punch, the element size is refined by both geometrical and equivalent plastic strain Fig. 9 (b-d). The fully damage elements appear firstly at the region which contacts with punch corner Fig. 9b. The macro-crack generates from this corner and propagates along the shear edge perpendicularly Fig. 9c. Finally, the shear edge forms when the macro-crack penetrates through the sheet and the copper sheet was cut, as shown in Fig. 9d when the punch penetration reached to $U_f = 0.33\text{mm}$.

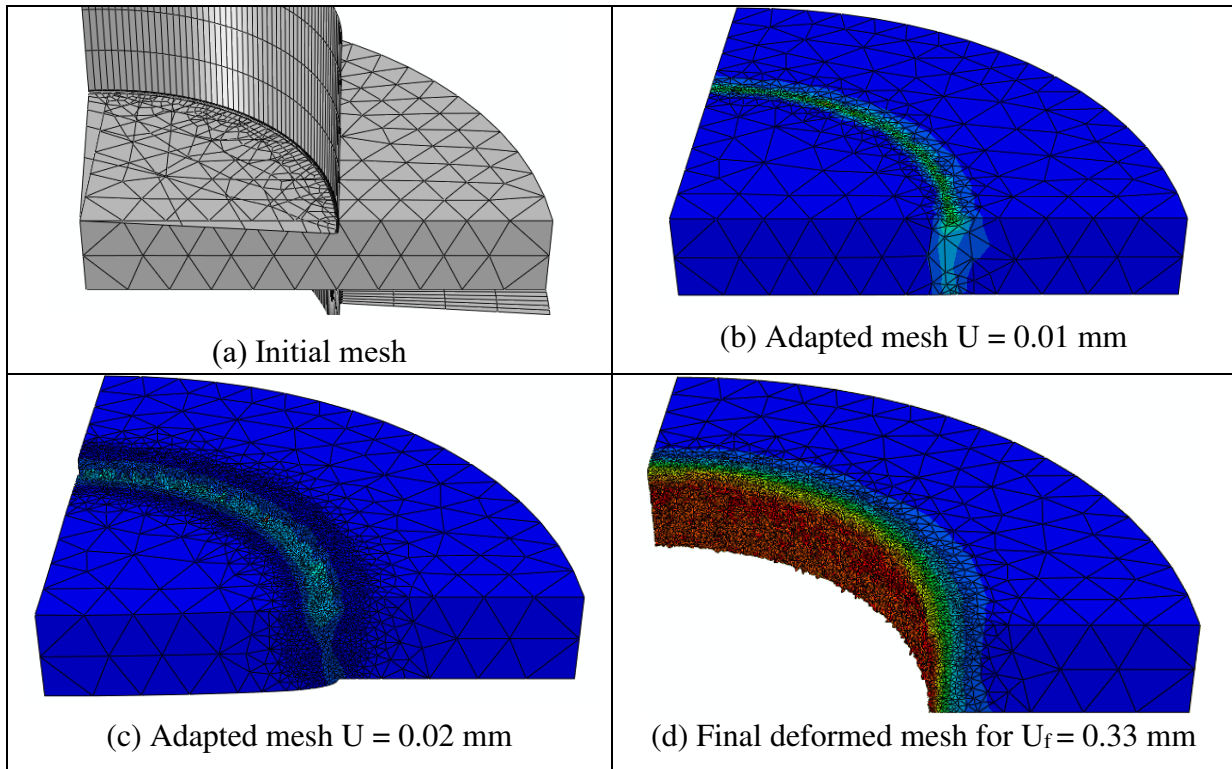


Figure 9. Predicted circular disc blanking using adaptive mesh

The morphology of sheared edge forms just in the fully damaged region, where the equivalent stress degrades to zero and corresponding to killed element. The predicted morphology using both the proposed model with and without adaptive remeshing scheme are compared to the experimental edge obtained by scanning electron microscopy analysis Husson [51] (see Fig. 10). It is clear that the profile of sheared edge (rollover, burnish and fracture) predicted by adaptive remeshing scheme (middle) is closer to the experiment one (right). Against in the case of a model without remeshing procedure the sheared edge profile obtained remains unrepresentative of the experimental result. For these results, we can nothing that only the adaptive remeshing scheme is able to predict the sheared edge profile of sheet cutting (see Table 4). In the industrial situation, the punch force and the punch penetration at fracture are important for tool and machine dimensioning. The shape of the cut edge

and the burr height are crucial for the final product quality. The prediction of these parameters by numerical adaptive simulation may be very helpful in blanked or sheared part design.

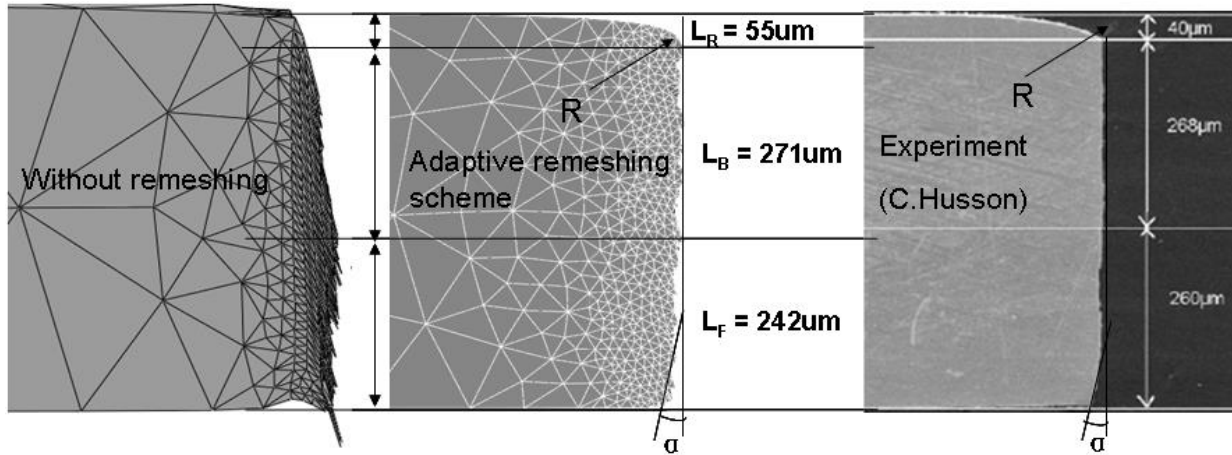


Figure 10. Experimental and predicted sheared edges profile with and without remeshing

Fig. 11 shows the computed blanking force versus the punch displacement obtained with /without adaptive remeshing in comparison with the experiment results. Note that the predicted result without adaptive remeshing deviates to the experiment values more and more severely with the increasing of the punch displacement. These differences are due essentially to the qualities of finite elements despite the used large number of elements (230 150) and to the convergence of the computational procedure (Table 4). Also notes that the overall error is very high (19.0%) in the case without remeshing with significant time calculations (3h 48min).

In the case of adaptive remeshing procedure, the predicted curve fitted the experiment values with a maximum force of $F_{max} = 3235N$ (experimental value $F_{max} = 3353N$) and displacement at fracture $U_f=0.34mm$ (experimental value $U_f = 0.36mm$). Also notes that in this case using a number of elements not high (54 519), the overall error is very smaller (1.23%) with relatively correct time calculation (2h 17min) (see Table 5).

Table 4: Computation time with and without remeshing

	Element number	CPU (hours)	Global error estimation
Without remeshing	230 150	3h 48min	0.1932
With remeshing	54 519	2h 17min	0.0123

Table 5: Computed blanking force; punch displacement and edge profile of sheet cutting

	F_{max} (N)	U_f (mm)	α	R (mm)	L_R (μm)	L_B (μm)	L_F (μm)	L_{Burr} (μm)
Without remeshing	6640	0.53	-	0.65	56.5	270	248	55
With	3235	0.35	7°	0.53	55	271	242	0

remeshing								
Experiment	3353	0.36	5°	0.50	40	268	260	0

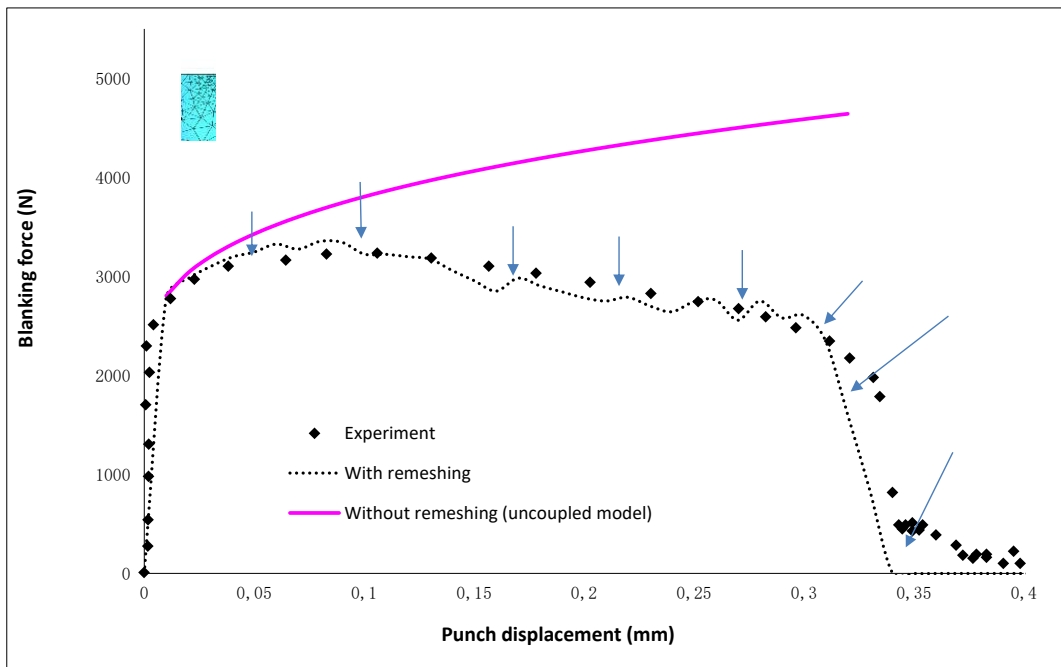


Figure 11. Predicted blanking force versus punch displacement coupled and uncoupled model

Based on this finite element model, the simulations of blanking processes with the effects of numerical and technical parameters are investigated in this section. Four process parameters will be studied numerically:

- (1) Mesh size : $H_{\min} = 0.2\text{mm}$ (Coarse mesh); $H_{\min} = 0.15\text{mm}$ (moderate coarse) and $H_{\min} = 0.1\text{mm}$ (Fine mesh)
- (2) Tools wear : $R = r = 1.0\text{ mm}$ (Worn tools), $R = r = 0.4\text{mm}$ (Moderate worn tools) and $R = r = 0.2\text{ mm}$ (Sharp tools)
- (3) Punch-die clearance : $c / t = 0\%$ (Zero), $c/t = 4\%$ (Small) and $c/t = 20\%$ (Large)
- (4) Tool deformability : Punch and die are rigid, Punch is rigid and die is deformable and Punch and die are deformable

5.2.1. Mesh size effect

For maximum numerical efficiency, a mesh should be refined near regions of interest with high damage localization and coarsened far from the regions of interest. A geometry-dependent element sizing function to determine local element sizes. The user controls the element sizing function via a set of user-provided parameters δ .

Figure 12 presents different remeshing step at each punch displacement. Noting that the adapted mesh of the work-piece to the geometry of punch and to the physical plastic strain deformation localization. The blanking process can also be investigated by monitoring the changes in the blanking force during the blanking process. The responses of blanking force-displacement for adaptive remeshing procedure using $H_{\min} = 0.1\text{mm}$, 0.15mm and 0.2mm are presented in Fig 13. The predicted maximum blanking force was a little higher in the model of fine mesh (12.4kN) than that of relative coarse mesh (12kN). As the same time, the punch needs more displacement (0.2mm) in the model of $H_{\min} = 0.1\text{mm}$ than that in the model using $H_{\min}=0.2\text{mm}$ to finish the final blanking. These prove again that the damage evolves quicker in the mesh of smaller size elements. Hence, it is better to choose a suitable mesh size according to the response of blanking force and displacement in experiment before creating the finite element model for blanking simulation. In this paper, the minimum mesh size of $H_{\min} = 0.1\text{mm}$ is used to study the effects of tool wear and clearance. Also notes that in this case using a fine mesh size $H_{\min} = 0.1\text{mm}$, the overall error is smaller (5.5%) with relatively correct time calculation (3h 30min) (see Table 6).

The sheared edges are formed with the different morphologies in these three models. Generally, the characteristic depths of sheared edge includes: Rollover, Burnish, Fracture and Burr. These characteristic depths of sheared edge can reflect the blanking quality directly, and it is preferred to have a large shear zone and smaller burr (see Table 7). As shown in Fig. 12, these characteristic depth have no obvious differences in these three model but the model with smaller minimum mesh size has a better performance on predicting the burnished region caused by shear damage.

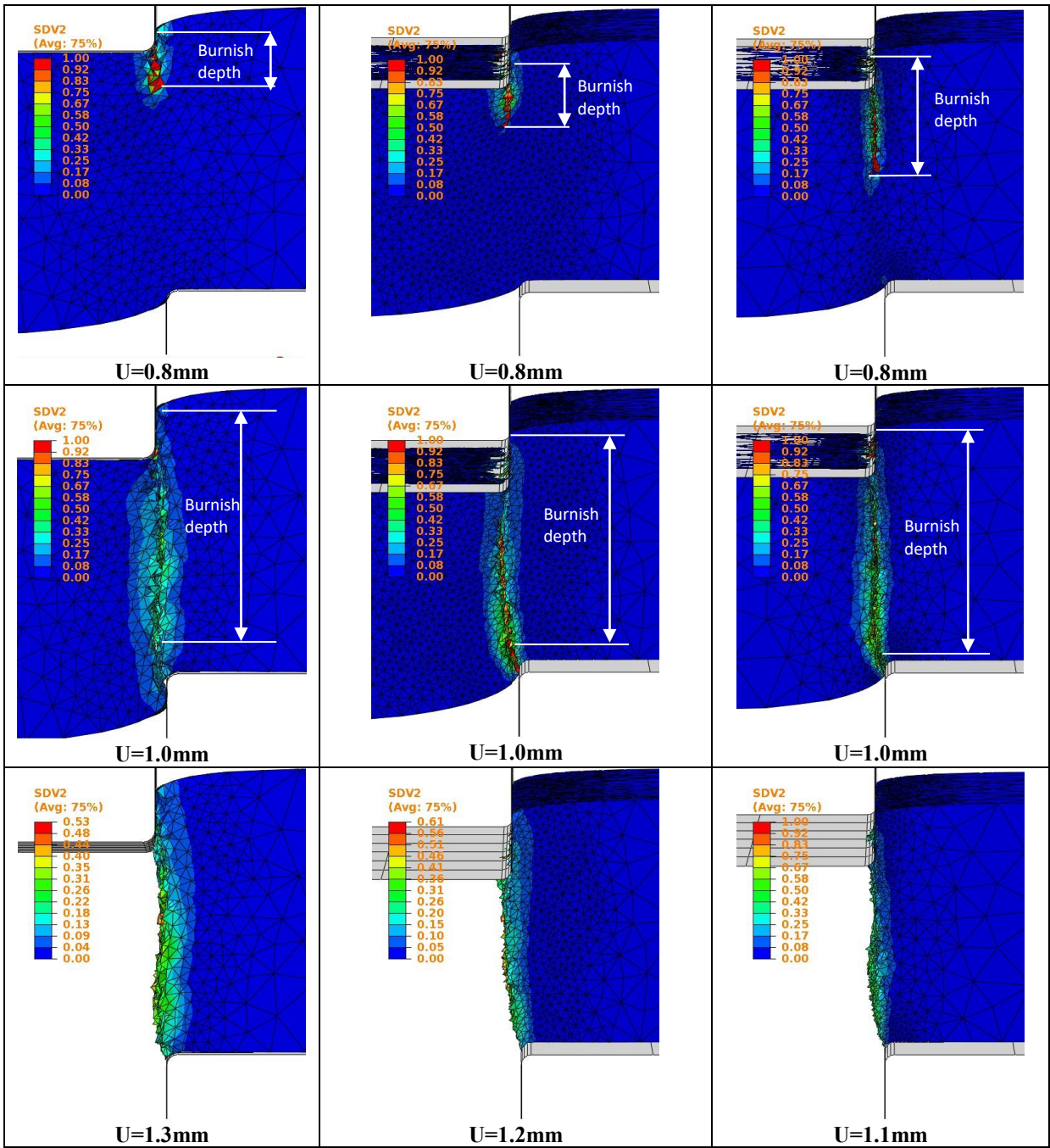
To avoid the effects of mesh size in numerical aspects, nonlocal method is recommended and it has been discussed a lot in literatures [54-66].

Table 6. Computational time for different mesh size

H_{\min} (mm)	Element number	CPU (hours)	Global error estimation
0.20	45 230	1h 48min	0.750
0.15	90 065	2h 37min	0.237
0.10	135 067	3h 30min	0.055

Table 7. Blanking force, displacement and sheared edge characteristics for different mesh size

H_{\min} (mm)	F_{\max} (kN)	U_f (mm)	α	R (mm)	L_R (μm)	L_B (μm)	L_F (μm)	L_{Burr} (μm)
0.20	12.42	1.3	3°	0.60	58	270	252	25
0.15	12.38	1.2	7°	0.53	55	271	242	50
0.10	12.00	1.0	3°	0.57	60	270	280	0



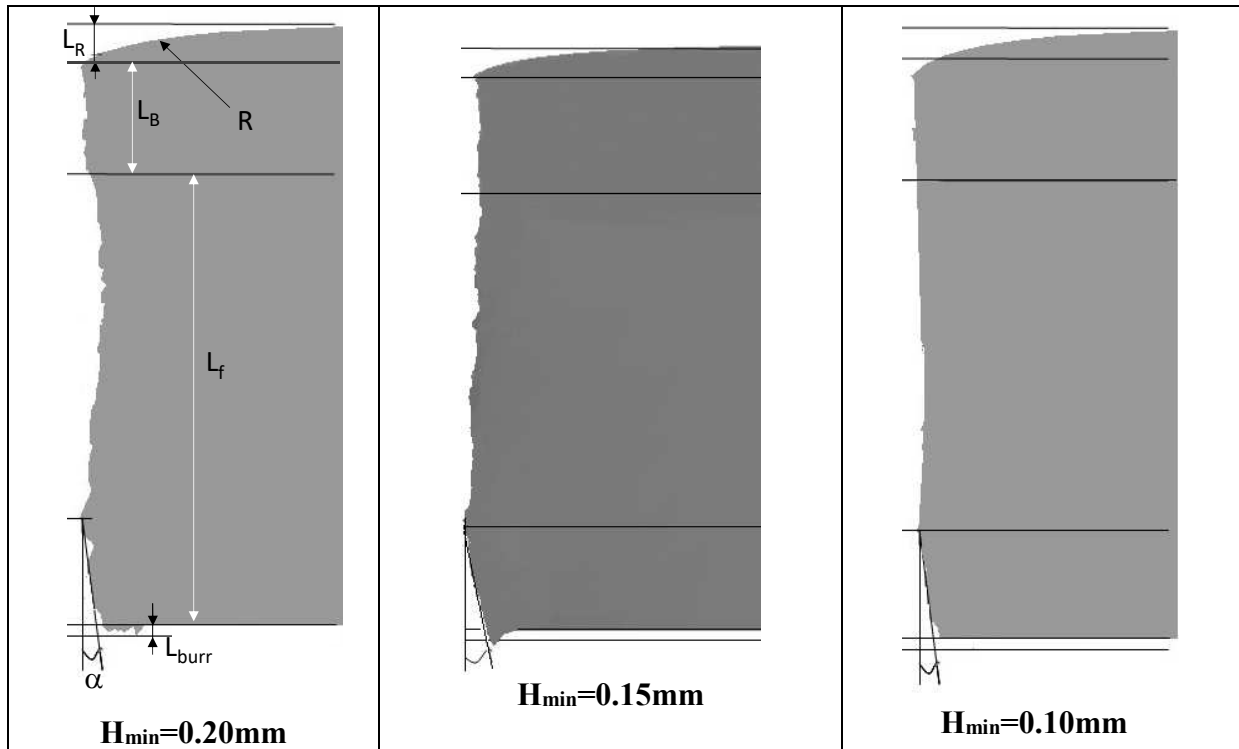


Figure 12. Damage initiation and propagation for different mesh size

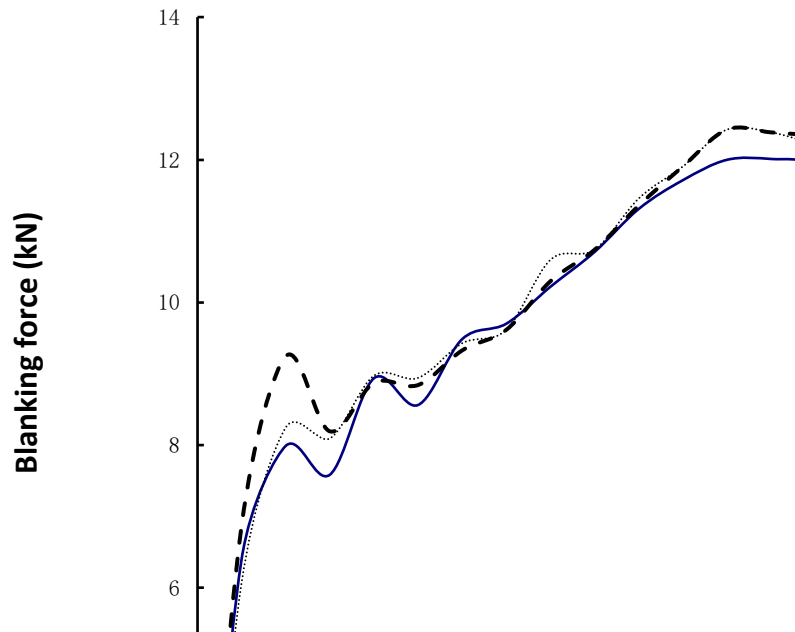


Figure 13. Predicted blanking force versus punch displacement effect of mesh size

5.3. Tool wear effects

This section is focused on the parametric study in order to predict the influence of the tools wear on the blanking product quality. The phenomenon of the friction between tools and sheet metal can cause tool wear. The external surface of the tools is always worn and degraded for this phenomenon, especially on the corner of tools. Tool wear influence can be accounted in numerical simulation by changing the values of punch and die corner radius [51]. In practice, the new tool has the sharp edges

whose corner radius is small. After sometimes using, the tools wear into dull edges whose corner radius increase. The sharp tool always achieves the fine quality of sheared edge and dull tool is contrary.

In this study, the punch angle radius R and the die angle radius r , are changed in order to model the tool edge cutting. The cutting edge with radius of $R=r=10\mu\text{m}$ represents new punch and die while $R_P=R_D=40\mu\text{m}$ represents "moderate" worn tools and $R_P=R_D=100\mu\text{m}$ represents much worn tools. The friction coefficient estimated at $\mu=0.02$ which corresponds to the good lubrication and the tool clearance is chosen as 2.5%. The blanking force in new, moderate and worn tools are presented in Fig. 13. It can clearly observe that, to achieve the complete blanking operation, worn tools need the bigger (40% higher) punch displacement as compared with new ones. The 6% additional maximum blanking force consumes with worn tool as the same time. The punch entry depth U_f at fracture (corresponding to zero force) and more results are summarized in Table 6. To the predicted morphology of sheared edges, as shown in Fig. 14, it is obviously that sharp edges obtained the fine quality of sheared edge using new tools than that of dull edges obtained with worn tools. The characteristic depth of sheared edge has changed a lot when worn tools are used, especially, the rollover and burnishing depth increases a lot and the fracture depth decrease. The small radius of rollover and large fracture angle directly reflect the bad part edge quality in blanking with worn tools. Simultaneously, the burr generates easily when tools are worn, which is harmful to blanking industrials (see Table 8).

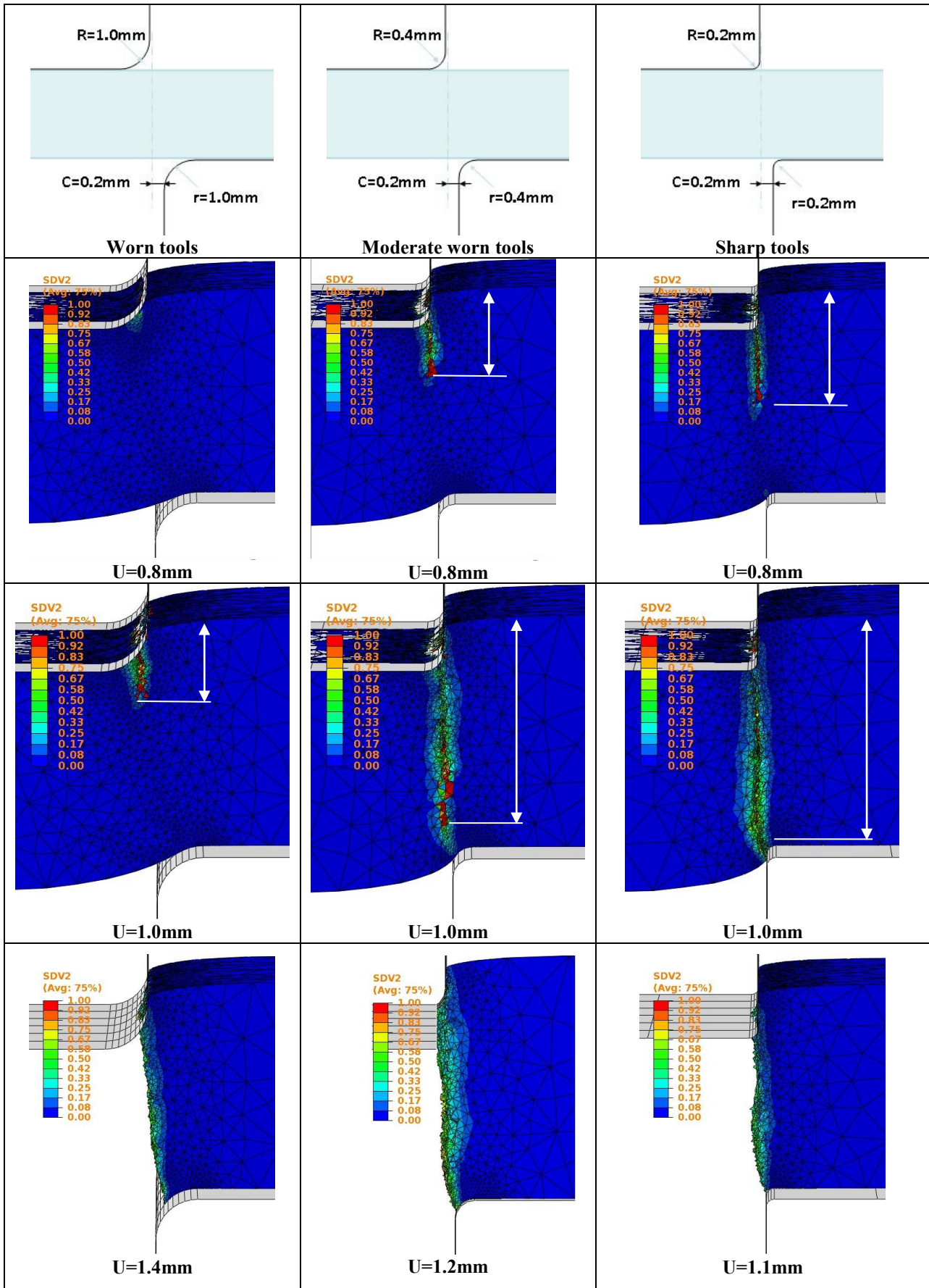
Tool wear is caused by the phenomenon of the friction between tools and sheet metal. The external surface of the tool is always worn and degraded for this phenomenon, especially on the corner of tools. The effect of tool wear on part edge quality is significant [56-60]. Tool wear leads to the formation of burrs and increases burr length. Burr length is generally an important criterion in the industry to evaluate part quality. Burr length indicates when the tool should be reground to obtain the sharp die and punch radius. Tool wear also induces large fracture angle which can reduce blanking quality. Tool wear can be estimated using finite element simulations by theoretically increasing the punch and die corner radii in simulations.

As illustrated in Fig. 14, the crack generates and propagates most rapidly in the blanking model using the new tool blanking when punch moves to $U=0.8\text{mm}$. The final blank is produced when punch moves to $U_f=1.1\text{mm}$ in the new tool blanking, $U_f=1.2\text{mm}$ in moderate worn tool blanking and $U_f=1.4\text{mm}$ in worn tool blanking. The characteristic depths of sheared edge (rollover, Burnish, Fracture and Burr) can be used to evaluate the blanking quality. Practically, it is preferred to have a large shear zone and smaller burr. The predicted blanking force responses in these models are presented in Fig.15. It can be clearly observed that, to achieve the complete blanking operation, worn

tools need the longer punch displacement ($U_f=1.4\text{mm}$) compared with the new one ($U_f=1.1\text{mm}$) and the moderate worn one ($U_f=1.2\text{mm}$). At the same time, the 9% additional maximum blanking force consumes with worn tool during the sheet metal blanking. The simulation results show us that the new tool blanking is helpful to generate the good quality products.

Table 8. Blanking force, displacement and characteristic depths of sheared edge for different tool wear conditions

R=r (mm)	F_{\max} (kN)	U_f (mm)	α	L_R (mm)	L_B (mm)	L_F (mm)	L_{Burr} (mm)
0.2	12.06	1.1	6.2°	0.055	0.271	0.242	0.011
0.4	12.60	1.2	10.9°	0.070	0.316	0.182	0.023
1.0	13.11	1.40	18.4°	0.087	0.345	0.136	0.045



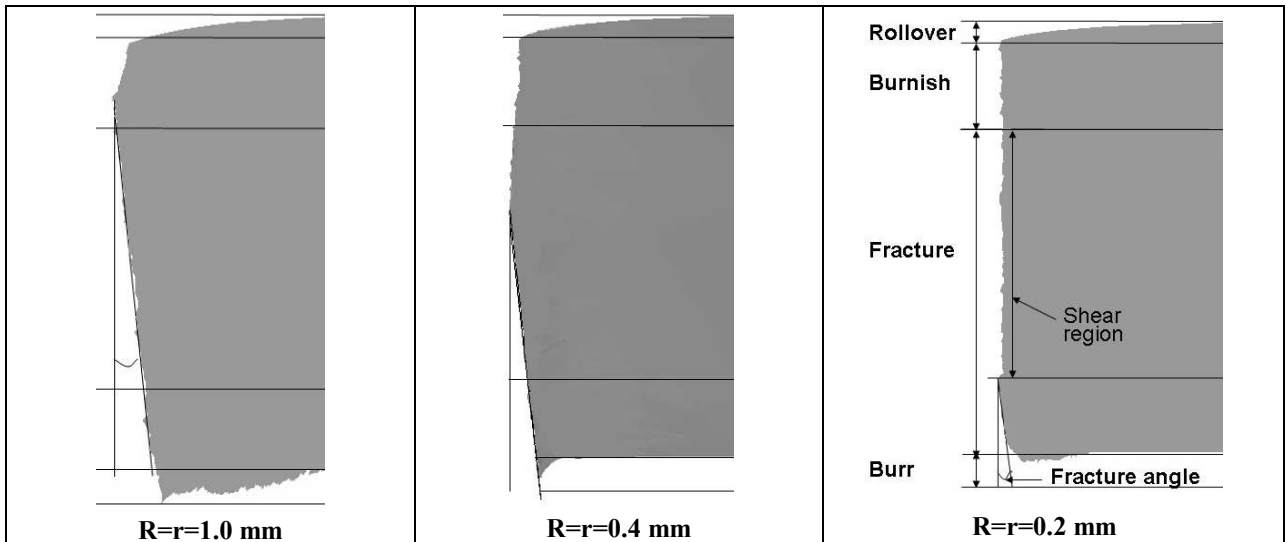


Figure 14. Damage initiation and propagation for different tool wear

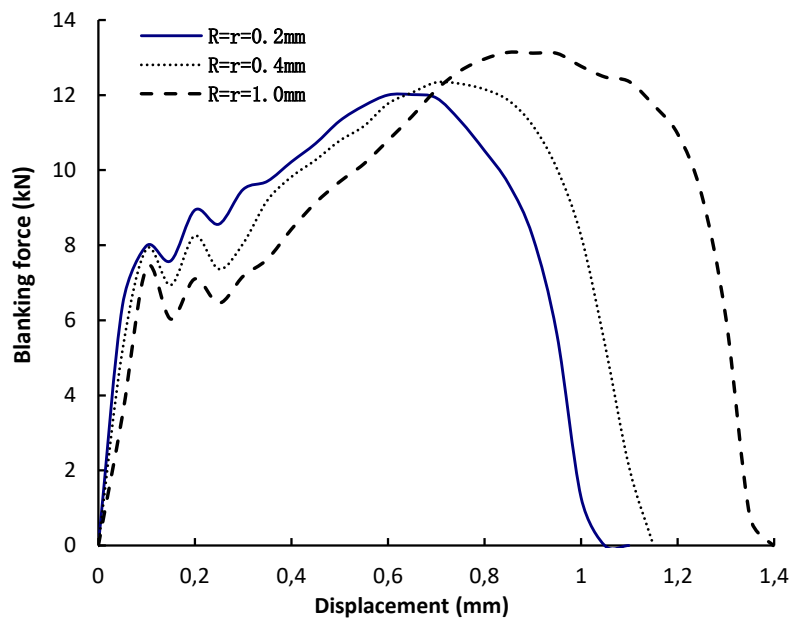


Figure 15. Predicted blanking force versus punch displacement effect of tool wear

5.4 Effect of tools clearance

Punch-die clearance plays an important role in the quality of sheet metal blanking process [59, 61-66]. Clearance is the gap between the punch and the die, which is also represented by the ratio of this gap and sheet thickness (c/t). Clearance (distance between the punch and die) in sheet metal cutting is ranged between 4% and 8% of stock thickness. If too small, fracture lines pass each other, causing double burnishing and larger force and if too large, metal is pinched between cutting edges and excessive burr results. Recommended allowance is determined according to type of metal:

- $c/t = 4.5\%$ for aluminum alloys.

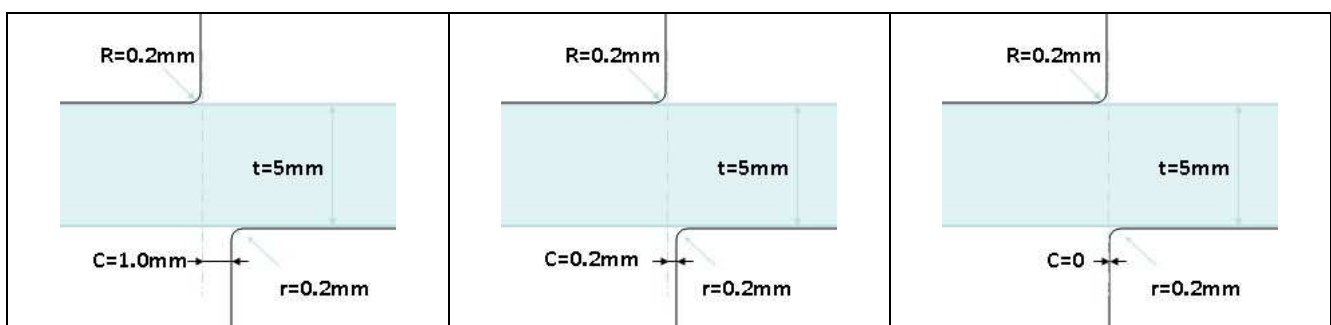
- $c/t = 6.0\%$ for brass, soft cold rolled steel, soft stainless steel.
- $c/t = 7.5\%$ for cold rolled steel, half hard; stainless steel, half hard.

Practically, if the clearance becomes large, although the force necessary for blanking will be small, the rollover of the cut cross-section and the inclination of the fracture cross-section shown will both become large. On the contrary, insufficient clearance produces secondary shear; that is, the cracks originating at the punch and die do not meet. Furthermore, tool life is also lowered by improper clearance. Hence, it is valuable to study the effect of clearance on sheet metal blanking.

The crack generation and propagation for no clearance ($c/t=0\%$) are presented in Fig. 14 (left), for small clearance ($c/t=4\%$) are presented in Fig. 14 (middle) and large clearance ($c/t = 20\%$) are presented in Fig. 14 (right). The final blank is produced when punch moves to $U_f=1.1\text{mm}$, 1.15mm and 1.3mm for zero, small and large clearance ratio respectively. It is clear that the crack has almost perpendicularly propagated in the metal sheet along the thickness direction in the zero clearance blanking, while the crack is inclined in the small and large clearances blanking. This makes the quality of shear edge become badly (large burr or high fracture angle) in large clearance blanking. Hence, it is recommended to choose a suitable small clearance to obtain a fine quality of shear edge.

The blanking force responses of different clearance blanking are presented in Fig.15. The results show that the blanking force decreases when the clearance increases. However, the larger clearance exists in blanking model, the longer punch displacement is needed to finish the blanking operation.

The clearance also has significant effects on the morphology of sheared edge. Excessive clearance causes large plastic deformation, large burr, and high fracture angle. As shown in Table 7, the burr is not formed and a very small fracture angle exists in the sheared edge of no clearance blanking model. However, these characteristic depths have changed a lot in the large clearance blanking model. The depth of rollover increases, the depth of burnish is not clear, and the depth of fracture has taken over the great mass of sheared edge. Besides these, a clear burr generates and a large fracture angle exists in the sheared edge of large clearance blanking model. Hence, it is recommended to choose a suitable small clearance to obtain a fine quality of cutted sheet.



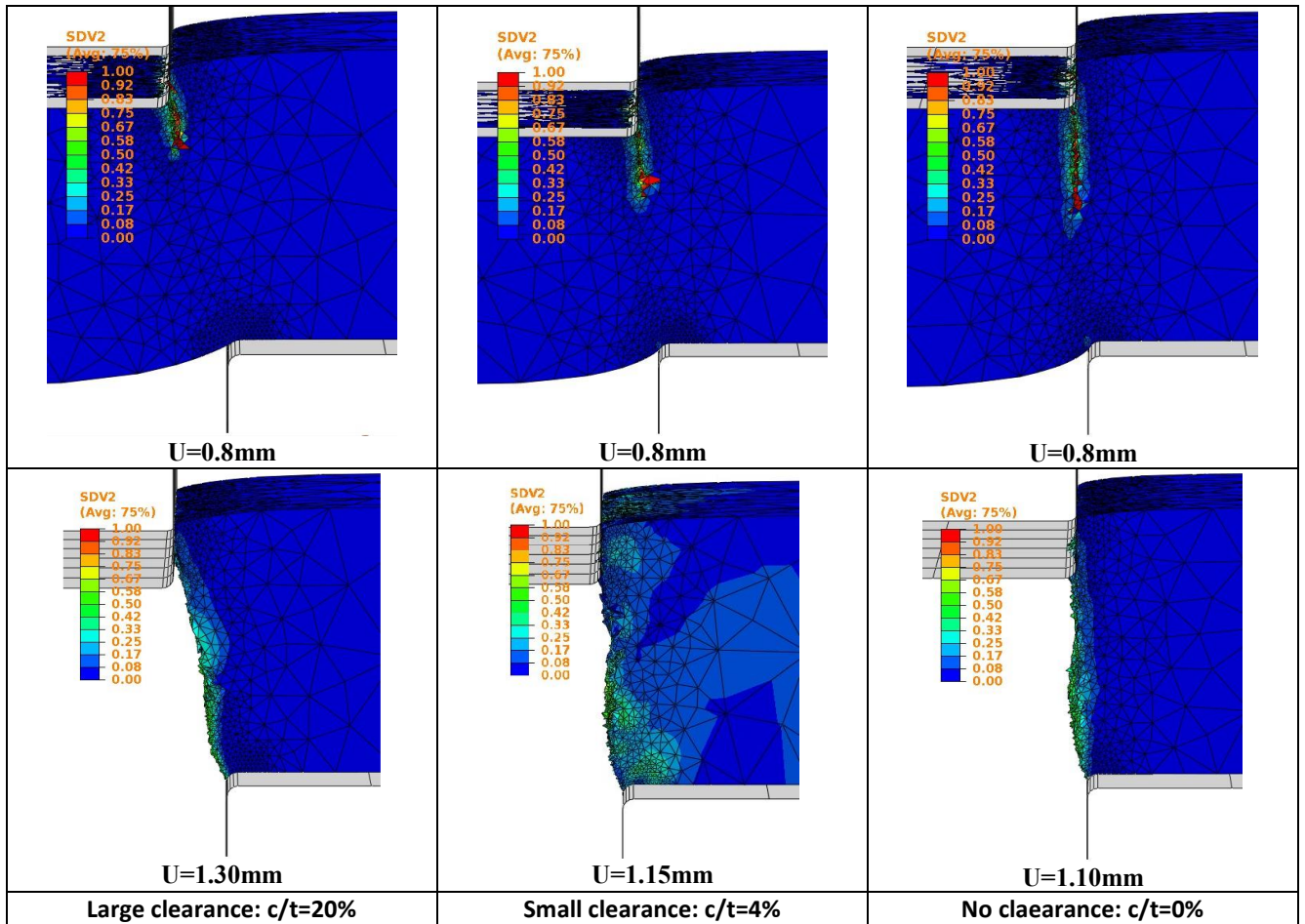


Figure 14. Damage initiation and propagation for different tool clearance

Table 7. Blanking force, displacement and the characteristic depths of sheared edge for different clearances conditions

c/t	F_{max} (kN)	U_f (mm)	α	R (mm)	L_R (mm)	L_B (mm)	L_F (mm)	L_{Burr} (mm)
0%	12	1.1	6.2°	0.62	0.055	0.271	0.242	0.00
4%	10.7	1.15	13.5°	0.49	0.080	0.302	0.186	0.50
20%	10.2	1.30	24.8°	0.28	0.120	0.331	0.117	0.60

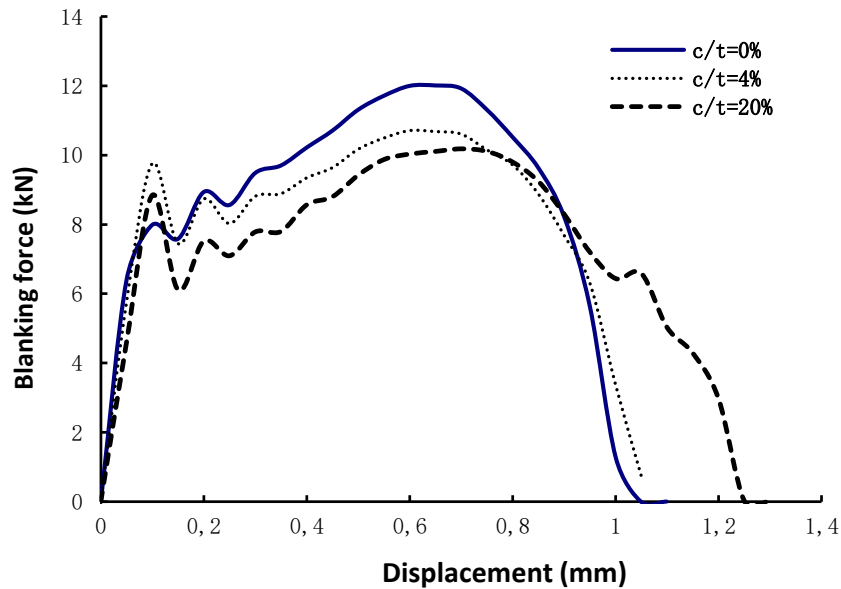


Figure 15. Predicted blanking force versus punch displacement effect for different tool clearances

5.5. Effect of tool's deformability

Practical experience shows, that the elastic tools (die and holder) and press (punch) deformations under load considerably affect the blanking results (sheared edge, residual stress, spring-back, blanking force,...). These deformations cause a gap between the punch at end of the stroke if the production punch has different elastic properties than the try-out press. The sheared part is not sufficiently formed unless an additional force is added to close the gap. Also the profile of the sheared surface is strongly influenced by the rigidity of tools. More tools are and the profile is the cutted edges are poor quality. As tool elastically increases, the material tends to be pulled into the die, rather than being sheared. A 3D elastic solid model is created to compare the result with rigid model. To predict the magnitude of the total force needed instead of standard rigid tools has be implemented. The disadvantage of the calculation method is a very high CPU time.

In order to study the effect of those deformations, the elastic properties of the punch and die must be considered during the cutting process. Three cases will be studied numerically. In the first case, the cylindrical punch and die are assumed elastic deformable ($E=700\text{GPa}$ and $\nu=0.23$), in the second case, the punch is supposed rigid and the die is elastic and in the last case, the punch is supposed elastic and the die is considered rigid. The deformable tools have been modelled with hexahedral finite elements (CD38R). The blanking parameters are: $R=r=10\mu\text{m}$, $c/t=2.5\%$ and $\mu=0.02$. A refined regular mesh is associated with the punch and die edges where will have highly stress distribution (Fig. 16).

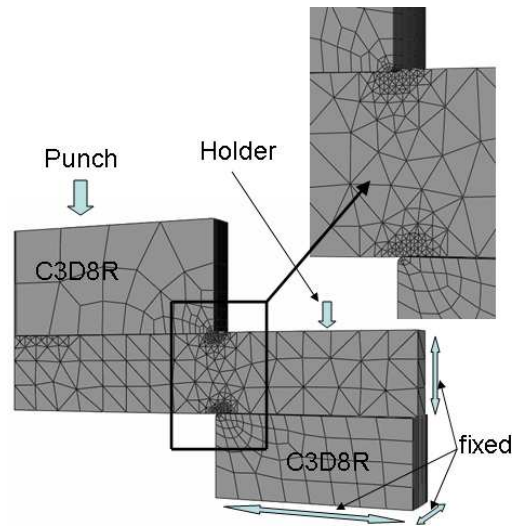


Figure 16. Finite element discretization of deformable blanking tools

The global response as the blanking force versus punch displacement obtained with deformable tools is presented and compared to the case of rigid tools in Figure 17. The results show the difference when deformation of the tools is taken into account. As expected, the cutting operation seems to be harder to perform with deformable tools. The maximum blanking force is 15% higher and the total punch displacement at the final fracture is 120% higher (Fig. 18). Also, the shape of the force-displacement curve obtained with deformable tools is quite different from the response of rigid tools.

	Experiment	Rigid tools	Elastic punch – Rigid die	Rigid punch – Elastic die	Deformable punch and die
Sheared edge profile					
F_{max} (N)	3353	3235	3588	3450	4047
U_f (mm)	0.36	0.35	0.42	0.37	0.48
α (°)	5	7	12	10.3	18.4
L_R (μm)	40	55	70	65	72
L_B (μm)	268	271	276	316	345
L_F (μm)	260	242	244	182	136
L_{Burr} (μm)	0	0	0	23	45

Figure 17. Blanking force, displacement and the characteristic depths of sheared edge for different tool cases

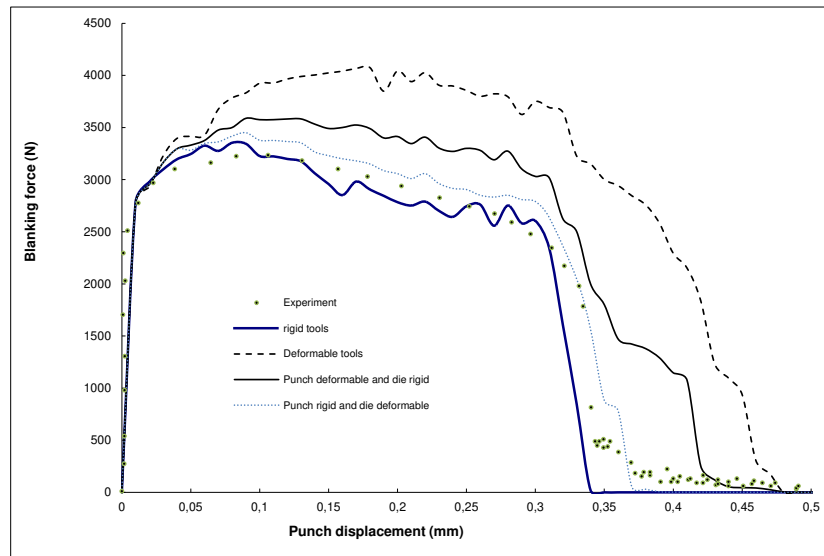
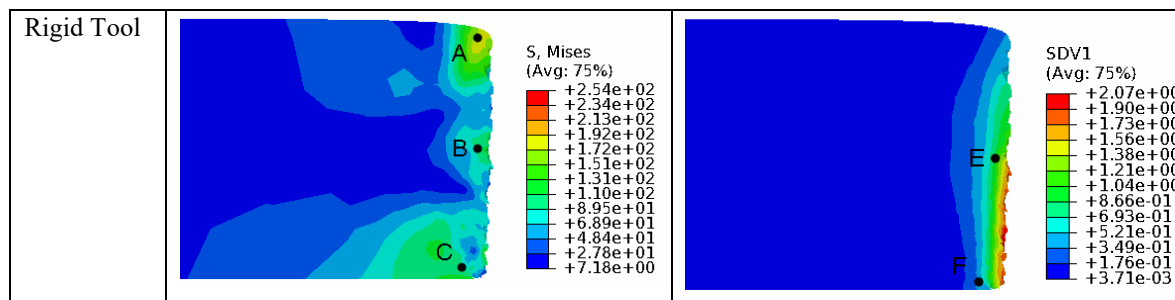


Figure 18. Predicted blanking force versus punch displacement effect for different tool cases

5.6. Residual stress distribution

The last one is the residual stress and strain in work-piece after blanking. Analyzing the residual stress and strain of both new tool and worn tool in Fig. 19, it is easily to understand the blanking mechanism. The residual stress in (a) and (c) have the clear distribution boundaries, which match with the morphology of sheared edge. For example, the point A, B and C which have the concentrated distributions of stress are the end of rollover, start of fracture and the end of fracture respectively in both figures (a) and (c). The positions of A, B and C can obviously describe the experience of damage in blanking process. Also, the concentrated distributions of residual strain existed in the shear fracture period from E to F. So, it is valuable to analyze the blanking mechanism through detecting the residual stress and strain.



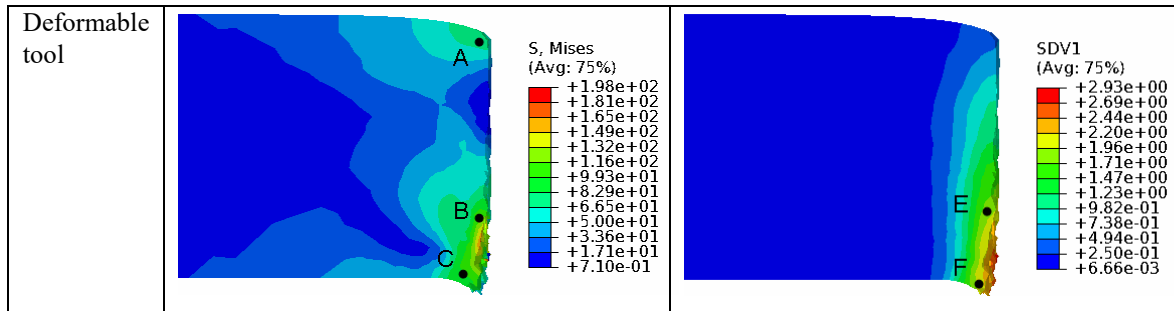


Figure 19. Residual stress and strain after blanking: new tool (left) and worn tool (right)

6. Conclusion

This paper develops a fully coupled elasto-viscoplastic and damage constitutive model based on the continuum damage mechanics. The multi-axial damage evolution is introduced into this model through using a stress state parameter. This parameter, the function of stress triaxiality and Lode angle, has the different value between zero and one according to the different states of stress. The material behavior of 2024-T351 aluminum is predicted using this constitutive model. Experimental data in literatures are used to determine the stress state parameter and the model is validated in both tensile and compressive tests.

As the same time, a computation platform is constructed by coupling an advanced 3D adaptive remeshing procedure in this paper. It is based on tetrahedral element and has the ability to adaptively control the mesh size according to both the geometrical and the physical error estimates. The mesh quality is also automatically optimized during remeshing procedure. The convergence and accuracy of the simulation are greatly improved through using this adaptive remeshing procedure. The finite element model of sheet metal blanking is built based on the constitutive equation and adaptive remeshing procedure. The technical parameters of metal blanking are numerical studied including the tool ware and the clearance.

Corresponding author: Correspondence to Abel CHEROUAT

Authors' contributions: Abel CHEROUAT contributed to the conception of the study and wrote the manuscript; ZHANG Jie performed the data analyses and the experiment; Houman BOROUCHEKI helped perform the numerical analysis.

Consent for publication: The author confirms the publication of this paper has been approved by all coauthors, and its publication has been approved by the responsible authorities at the institution where the work is carried out.

Funding: The authors would like to thank the support of the UR-GAMMA3.

Institutional Review Board Statement: Not applicable.

Informed Consent Statement: Not applicable.

Availability of data and material: The data presented in this study are available on request from the corresponding authors.

Ethics approval: Not applicable.

Consent to participate: Not applicable.

Competing interests: The authors declare no competing interests.

Conflicts of Interest: The authors declare no conflict of interest.

References

- [1] Kachanov LM. Time of the rupture process under creep conditions. *Izv Akad Nauk {SSR} Otd Tech Nauk*. 1958;8:26-31.
- [2] McClintock FA. A Criterion for Ductile Fracture by the Growth of Holes. *Journal of Applied Mechanics*. 1968;35:363-71.
- [3] Rice JR, Tracey DM. On the ductile enlargement of voids in triaxial stress fields. *Journal of the Mechanics and Physics of Solids*. 1969;17:201-17.
- [4] Gurson AL. Continuum Theory of Ductile Rupture by Void Nucleation and Growth: Part I---Yield Criteria and Flow Rules for Porous Ductile Media. *Journal of Engineering Materials and Technology*. 1977;99:2-15.
- [5] Besson J (2010) Continuum models of ductile fracture: a review. *Int J Damage Mech* 19(1):3–52
- [6] Chaboche JL. Anisotropic creep damage in the framework of continuum damage mechanics. *Nuclear Engineering and Design*. 1984;79:309-19.
- [7] Lemaitre J. A Continuous Damage Mechanics Model for Ductile Fracture. *Journal of Engineering Materials and Technology*. 1985;107:83-9.
- [8] Benzerga AA, Leblond JB (2010) Ductile fracture by void growth to coalescence. *Adv Appl Mech* 44:169–305.
- [9] Atkins AG, Mai YW. Fracture strains in sheet metalforming and specific essential work of fracture. *Engineering Fracture Mechanics*. 1987;27:291-7.
- [10] Lou, Y, Yoon, JW (2017) Anisotropic ductile fracture criterion based on linear transformation. *International Journal of Plasticity* 93: 3–25.
- [11] Badreddine, H, Saanouni, K (2017) On the full coupling of plastic anisotropy and anisotropic ductile damage under finite strains. *International Journal of Damage Mechanics* 26(7): 1080–1123.
- [12] Steglich D, Brocks W, Heerens J, Pardoen T. Anisotropic ductile fracture of Al 2024 alloys. *Engineering Fracture Mechanics*. 2008;75:3692-706.
- [13] Xue L, Wierzbicki T. Ductile fracture initiation and propagation modeling using damage plasticity theory. *Engineering Fracture Mechanics*. 2008;75:3276-93.
- [14] Yoon JH, Stewart JB, Cazacu O. Coupled elastic–plastic damage model for a porous aggregate with an incompressible matrix displaying tension–compression asymmetry. *Engineering Fracture Mechanics*. 2011;78:1407-23.
- [15] Bonora N, Gentile D, Pirondi A, Newaz G. Ductile damage evolution under triaxial state of stress: theory and experiments. *International Journal of Plasticity*. 2005;21:981-1007.
- [16] Needleman A, Tvergaard V. An analysis of ductile rupture in notched bars. *Journal of the Mechanics and Physics of Solids*. 1984;32:461-90.
- [17] Bonfoh N, Lipinski P, Carmasol A, Tiem S. Micromechanical modeling of ductile damage of polycrystalline materials with heterogeneous particles. *International Journal of Plasticity*. 2004;20:85-106.
- [18] Tvergaard V, Niordson C. Nonlocal plasticity effects on interaction of different size voids. *International Journal of Plasticity*. 2004;20:107-20.
- [19] A.E. Tekkaya, P.-O. Bouchard, S. Bruschi, C.C. Tasan, Damage in metal forming *CIRP Annals* vol. 69, Issue 2, 2020, 600-623, <https://doi.org/10.1016/j.cirp.2020.05.005>
- [20] Brokken D, Brekelmans WAM, Baaijens FPT. Predicting the shape of blanked products: a finite element approach. *Journal of Materials Processing Technology*. 2000;103:51-6.

- [21] Zhu YY, Cescotto S, Habraken AM. A fully coupled elastoplastic damage modeling and fracture criteria in metalforming processes. *Journal of Materials Processing Technology*. 1992;32:197-204.
- [22] Brokken D, Brekelmans WAM, Baaijens FPT. Numerical modelling of the metal blanking process. *Journal of Materials Processing Technology*. 1998;83:192-9.
- [23] Stein E. A pioneer in the development of the finite element method in engineering science. *Steel Construction*. 2009;2:264-72.
- [24] Borouchaki H, George PL, Hecht Fdr, Laug P, Saltel E. Delaunay mesh generation governed by metric specifications. Part I. Algorithms. *Finite Elements in Analysis and Design*. 1997;25:61-83.
- [25] Borouchaki H, George PL, Mohammadi B. Delaunay mesh generation governed by metric specifications Part II. Applications. *Finite Elements in Analysis and Design*. 1997;25:85-109.
- [26] Borouchaki H. CD, George P.L., Laug P. and Frey P.J. Estimateurs d'erreur géométriques et adaptation de maillage: Hermès; 2001.
- [27] Borouchaki H, Cherouat A, Laug P, Saanouni K. Adaptive remeshing for ductile fracture prediction in metal forming. *Comptes Rendus Mécanique*. 2002;330:709-16.
- [28] Borouchaki H, Grosjes T, Barchiesi D. Enhancement of the accuracy of numerical field computation using an adaptive three-dimensional remeshing scheme. *Comptes Rendus Mécanique*. 2010;338:127-31.
- [29] Borouchaki H, Grosjes T, Barchiesi D. Improved 3D adaptive remeshing scheme applied in high electromagnetic field gradient computation. *Finite Elements in Analysis and Design*. 2010;46:84-95.
- [30] Borouchaki H, Grosjes T, Barchiesi D. Enhancement of the accuracy of numerical field computation using an adaptive three-dimensional remeshing scheme. *Comptes Rendus Mécanique*. 2010;338:127-31.
- [31] Cherouat A., Borouchaki H. and Zhang J., Simulation of Sheet Metal Forming Processes Using a Fully Rheological-Damage Constitutive Model Coupling and a Specific 3D Remeshing Method, *Metals* 2018, 8, 991; doi:10.3390/met8120991.
- [32] Lemaitre J. Coupled elasto-plasticity and damage constitutive equations. *Computer Methods in Applied Mechanics and Engineering*. 1985;51:31-49.
- [33] Chaboche JL, Cailletaud G. Integration methods for complex plastic constitutive equations. *Computer Methods in Applied Mechanics and Engineering*. 1996;133:125-55.
- [34] Saanouni K, Belamri N, Khelifa M, Badreddine H, Cherouat A, Bathe KJ. Finite anisotropic plastic flow with ductile damage for sheet metal forming simulation. *Computational Fluid and Solid Mechanics* 2003. Oxford: Elsevier Science Ltd; 2003. p. 611-4.
- [35] Perzyna P. Fundamental problems in viscoplasticity. *Advances in applied mechanics*. 1966;9:244-368.
- [36] Batra R C, Kim C. H G. Effect of viscoplastic flow rules on the initiation and growth of shear bands at high strain rates. Kidlington, ROYAUME-UNI: Elsevier; 1990. p. 859-74.
- [37] Johnson GR, Cook WH. Fracture characteristics of three metals subjected to various strains, strain rates, temperatures and pressures. *Engineering Fracture Mechanics*. 1985;21:31-48.
- [38] Fleck NA. Finite element analysis of plasticity-induced crack closure under plane strain conditions. *Engineering Fracture Mechanics*. 1986;25:441-9.
- [39] Lemaitre J. *A course on Damage Mechanics*. New York: Springer-Verlag; 1992.
- [40] Yu HL, Jeong DY. Application of a stress triaxiality dependent fracture criterion in the finite element analysis of unnotched Charpy specimens. *Theoretical and Applied Fracture Mechanics*. 2010;54:54-62.
- [41] Kweon S. Damage at negative triaxiality. *European Journal of Mechanics - A/Solids*. 2012;31:203-12.
- [42] Malcher L, Andrade Pires FM, César de Sá JMA. An assessment of isotropic constitutive models for ductile fracture under high and low stress triaxiality. *International Journal of Plasticity*. 2012;30–31:81-115.
- [43] Simo JC, Taylor RL. Consistent tangent operators for rate-independent elastoplasticity. *Computer Methods in Applied Mechanics and Engineering*. 1985;48:101-18.
- [44] Simo JC, Taylor RL, Pister KS. Variational and projection methods for the volume constraint in finite deformation elastoplasticity. *Computer Methods in Applied Mechanics and Engineering*. 1985;51:177-208.
- [45] Simo JC, Ju JW. Strain- and stress-based continuum damage models—I. Formulation. *International Journal of Solids and Structures*. 1987;23:821-40.
- [46] Ortiz M, Popov EP. Accuracy and stability of integration algorithms for elastoplastic constitutive relations, *International Journal for Numerical Methods in Engineering*. 1985;21:1561-76.
- [47] Simo JC, Hughes T.J.R. *Computational inelasticity* New York: Springer; 1998.
- [48] De Souza Neto EA, Perić D, Owen DRJ. *Computational Methods for Plasticity*: John Wiley & Sons, Ltd; 2008.
- [49] El khaoulani R, Bouchard PO. An anisotropic mesh adaptation strategy for damage and failure in ductile materials. *Finite Elements in Analysis and Design*. 2012;59:1-10.
- [50] A. Cherouat, H. Borouchaki and J. Zhang, Simulation of Sheet Metal Forming Processes Using a Fully Rheological-Damage Constitutive Model Coupling and a Specific 3D Remeshing Method , *Metals* 2018, 8(12), 991; <https://doi.org/10.3390/met8120991> - 26 Nov 2018
- [51] Qiao-Min Li, Zhao-Wei Yi, Yu-Qi Liu, Xue-Feng Tang, Wei Jiang and Hong-Jun Li, Explicit Analysis of Sheet Metal Forming Processes Using Solid-Shell Elements, *Metals* 2022, 12(1), 52; <https://doi.org/10.3390/met12010052>
- [52] B. Zeramdini, C. Robert, G. Germain, T. Pottier; Numerical simulation of metal forming processes with 3D adaptive Remeshing strategy based on a posteriori error estimation, *International Journal of Material Forming*, Issue 3/2019
- [53] Bao Y. Prediction of Ductile Crack Formation in Uncracked Bodies: Massachusetts Institute of Technology; 2003.
- [54] Wierzbicki T, Bao Y, Lee Y-W, Bai Y. Calibration and evaluation of seven fracture models. *International Journal of Mechanical Sciences*. 2005;47:719-43.
- [55] Bai Y. Effect of Loading History on Necking and Fracture: Massachusetts Institute of Technology; 2008.
- [56] Falconnet E, Makich H, Chambert J, Monteil G, Picart P. Numerical and experimental analyses of punch wear in the blanking of copper alloy thin sheet. *Wear*. 2012;296:598-606.
- [57] Shivpuri R, Singh S, Agarwal K, Liu C. Energy release rate based approach for the wear of punches in precision blanking of high strength steel. *CIRP Annals - Manufacturing Technology*. 2011;60:307-10.

- [58] Hernández JJ, Franco P, Estrems M, Faura F. Modelling and experimental analysis of the effects of tool wear on form errors in stainless steel blanking. *Journal of Materials Processing Technology*. 2006;180:143-50.
- [59] Hatanaka N, Yamaguchi K, Takakura N, Iizuka T. Simulation of sheared edge formation process in blanking of sheet metals. *Journal of Materials Processing Technology*. 2003;140:628-34.
- [60] Klocke F, Sweeney K, Raedt HW. Improved tool design for fine blanking through the application of numerical modeling techniques. *Journal of Materials Processing Technology*. 2001;115:70-5.
- [61] Fan WF, Li JH. An investigation on the damage of AISI-1045 and AISI-1025 steels in fine-blanking with negative clearance. *Materials Science and Engineering: A*. 2009;499:248-51.
- [62] Husson C, Correia JPM, Daridon L, Ahzi S. Finite elements simulations of thin copper sheets blanking: Study of blanking parameters on sheared edge quality. *Journal of Materials Processing Technology*. 2008;199:74-83.
- [63] Tekiner Z, Nalbant M, Gürün H. An experimental study for the effect of different clearances on burr, smooth-sheared and blanking force on aluminium sheet metal. *Materials & Design*. 2006;27:1134-8.
- [64] Hambli R, Guerin F. Application of a neural network for optimum clearance prediction in sheet metal blanking processes. *Finite Elements in Analysis and Design*. 2003;39:1039-52.
- [65] Fang G, Zeng P, Lou L. Finite element simulation of the effect of clearance on the forming quality in the blanking process. *Journal of Materials Processing Technology*. 2002;122:249-54.
- [66] Popat PB, Ghosh A, Kishore NN. Theoretical investigation of optimum clearance in blanking. *Journal of Mechanical Working Technology*. 1989;19:251-9.